

The quasar-galaxy cross SDSS J1320+1644: A probable large-separation lensed quasar¹

Cristian E. Rusu,^{2,3} Masamune Oguri,^{4,5} Masanori Iye,^{2,3,6} Naohisa Inada,⁷ Issha Kayo⁸
Min-Su Shin,⁹ Dominique Sluse¹⁰ and Michael A. Strauss¹¹

ABSTRACT

We report the discovery of a pair of quasars at $z = 1.487$, with a separation of $8''.585 \pm 0''.002$. Subaru Telescope infrared imaging reveals the presence of an elliptical and a disk-like galaxy located almost symmetrically between the quasars, creating a cross-like configuration. Based on absorption lines in the quasar spectra and the colors of the galaxies, we estimate that both galaxies are located at redshift $z = 0.899$. This, as well as the similarity of the quasar spectra, suggests that the system is a single quasar multiply imaged by a galaxy group or cluster acting as a gravitational lens, although the possibility of a binary quasar cannot be fully excluded. We show that the gravitational lensing hypothesis implies these galaxies are not isolated, but must be embedded in a dark matter halo of

¹Based on data collected at Subaru Telescope, which is operated by the National Astronomical Observatory of Japan. Use of the UH2.2 m telescope for the observations is supported by NAOJ.

²Optical and Infrared Astronomy Division, National Astronomical Observatory of Japan, 2-21-1, Osawa, Mitaka, Tokyo 181-8588, Japan.

³Department of Astronomy, Graduate School of Science, University of Tokyo 7-3-1, Hongo Bunkyo-ku, Tokyo 113-0033, Japan

⁴Kavli Institute for the Physics and Mathematics of the Universe, The University of Tokyo, 5-1-5 Kashiwanoha, Kashiwa, Chiba 277-8568, Japan.

⁵Division of Theoretical Astronomy, National Astronomical Observatory of Japan, 2-21-1, Osawa, Mitaka, Tokyo 181-8588, Japan.

⁶Department of Astronomical Science, The Graduate University for Advanced Studies (SOKENDAI), National Astronomical Observatory of Japan, 2-21-1, Osawa, Mitaka, Tokyo 181-8588, Japan

⁷Department of Physics, Nara National College of Technology, Yamatokohriyama, Nara 639-1080, Japan

⁸Department of Physics, Toho University, Funabashi, Chiba 274-8510, Japan.

⁹Department of Astronomy, University of Michigan, 500 Church Street, Ann Arbor, MI 48109-1042 USA.

¹⁰Argelander-Institut für Astronomie, Auf dem Hügel 71, 53121 Bonn, Germany.

¹¹Princeton University Observatory, Peyton Hall, Princeton, NJ 08544, USA.

virial mass $\sim 4 \times 10^{14} h_{70}^{-1} M_{\odot}$ assuming an NFW model with a concentration parameter of $c_{vir} = 6$, or a singular isothermal sphere profile with a velocity dispersion of $\sim 670 \text{ km s}^{-1}$. We place constraints on the location of the dark matter halo, as well as the velocity dispersions of the galaxies. In addition, we discuss the influence of differential reddening, microlensing and intrinsic variability on the quasar spectra and broadband photometry.

Subject headings: gravitational lensing: strong — binary quasars — quasars: individual (SDSS J132059.17+164402.59 & SDSS J132059.73+164405.6)

1. Introduction

Quasar pairs belong to one of three categories: gravitational lenses, binary quasars, and apparent (projected) pairs. Both components of a pair in the first two categories have the same redshift¹. Gravitationally lensed quasars dominate the small separation $\Delta\theta \lesssim 3''$ quasar pairs. These are produced by galaxy scale lenses, and for the past three decades have proven to be invaluable astrophysical and cosmological probes (e.g., Claeskens & Surdej 2002; Schneider et al. 2006). At larger separations, the lensing probability falls quickly (Turner et al. 1984), and becomes increasingly dominated by environmental effects due to galaxy groups and clusters (e.g., Keeton et al. 2000). The largest separation, double-image lensed quasar confirmed to date is Q0957+561 ($\Delta\theta = 6''.17$, Walsh et al. 1979), and the only other large separation lensed quasars known are the five-image SDSS J1004+4112 ($\Delta\theta = 14''.7$, Inada et al. 2003, 2005) and the three-image SDSS J1029+2623 ($\Delta\theta = 22''.5$, Inada et al. 2006; Oguri et al. 2008b). The two latter systems are lensed by clusters. Clearly, a larger sample is needed to study observationally the lensing probability distribution in the large-separation range (e.g., Oguri 2006; More et al. 2012). These wide lenses provide unique opportunities to study the interplay between baryonic and dark matter in groups ($\Delta\theta \lesssim 10''$), as well as the dark matter distribution in clusters² (e.g., Oguri et al. 2004).

Most large-separation quasar pairs known, however, are binary quasars (e.g., 19 pairs with $3'' < \Delta\theta < 10''$ in the sample of Hennawi et al. 2006). These are physically asso-

¹Small redshift differences in the components of binary quasar pairs, such as $661 \pm 173 \text{ km s}^{-1}$ for LBQS 0015+0239 (Impey et al. 2002), are consistent with the line-of-sight velocity difference of bound pairs of galaxies.

²It is worth mentioning that, in addition to lensed quasars, there are also many known lensed galaxies, with a large range of image separations, which we do not address here (e.g., Faure et al. 2008; Auger et al. 2009; More et al. 2012).

ciated quasars, in the sense that they are either gravitationally interacting, or belong to the same group or cluster. Binary quasars are found to be more abundant than predicted from extrapolating the quasar correlation function to small scales (e.g., Djorgovski 1991; Hewett et al. 1998; Hennawi et al. 2006; Kayo & Oguri 2012), which may imply that quasar activity is triggered and sustained by tidal interactions or mergers (e.g., Mortlock et al. 1999; Hopkins et al. 2005, 2006, 2007, 2008; Green et al. 2010, and references therein).

Many quasar pairs found in the range $3'' \lesssim \Delta\theta \lesssim 10''$ have proven difficult to classify as either lensed or binary quasars (e.g. Q2345+007; Weedman et al. 1982). In these systems no plausible lenses have been identified in the foreground, although the redshifts of the two components are identical and the spectra are quite similar. The spectra of gravitationally lensed images need not necessarily be identical, since they are prone to effects such as delayed intrinsic variability, chromatic microlensing, and differential extinction in the lensing galaxy (e.g., Wucknitz et al. 2003; Yonehara et al. 2008). On the other hand, there is little dynamic range in the spectral variation of quasars, meaning that pairs can have similar spectra by chance (e.g., Mortlock et al. 1999).

The suggestion of lensing by "dark" lenses (e.g., Koopmans 2000) or cosmic strings (Vilenkin 1984) has been put forward for these quasar pairs. There are in fact very few criteria for discriminating between the lensing and binary quasar hypotheses, without monitoring the luminosity variability of the components, in order to look for a time delay. Instead, clues about this population of pairs have been found statistically. For instance, it has been argued that most of these quasar pairs are not lensed quasars, based on comparisons of the optical and radio properties of the population (Kochanek et al. 1999). As for individual pairs, their nature must in general be estimated from the ensemble of their observed properties, and the accuracy of that estimation depends on the available observations.

In this paper, we report the discovery in the course of the Sloan Digital Sky Survey Quasar Lens Search (SQLS; Oguri et al. 2006, 2008a, 2012b; Inada et al. 2008, 2010, 2012) of a new large-separation ($\sim 8''.5$) quasar pair which has proven difficult to classify, SDSS J132059.17+164402.59 and SDSS J132059.73+164405.6 (hereafter jointly SDSS J1320+1644). In the near infrared, we detect two galaxies located between the quasars, producing an apparent cross-like configuration. In §2, we give a brief description of the lens candidate selection from the SDSS data, and in §3 we present our imaging and spectroscopic follow-up observations. Next, we estimate photometric redshifts for the two galaxies and show that they are located in the foreground (§4). We subsequently proceed with the gravitational lens mass modeling of this system (§5). In §6, we take a closer look at the quasar spectral differences, whereas in §7 we provide circumstantial evidence in favor of the lensing hypothesis. Finally, we summarize our conclusions in §8. Throughout this paper, we assume the concordance

cosmology with $H_0 = 70 h_{70} \text{ km}^{-1} \text{ s}^{-1} \text{ Mpc}^{-1}$, $\Omega_M = 0.27$ and $\Omega_\Lambda = 0.73$.

2. Discovery in the Sloan Digital Sky Survey

The Sloan Digital Sky Survey (SDSS-I, 2000-2005, SDSS-II, 2005-2008; York et al. 2000) is a combination of imaging and spectroscopic surveys which have mapped $\sim 10,000$ square degrees of the sky, centered at the North Galactic Cap. The observations are made at the Apache Point Observatory in New Mexico, USA, with a dedicated 2.5-meter wide-field telescope (Gunn et al. 2006). The imaging survey is conducted in five broad-band filters, centered at 3561 (u), 4676 (g), 6176 (r), 7494 (i), and 8873 Å (z) (Fukugita et al. 1996; Gunn et al. 1998; Doi et al. 2010). The automated pipeline reduction achieves an astrometric accuracy better than about $0''.1$ (Pier et al. 2003), and a photometric zero-point accuracy better than about 0.01 magnitude over the entire survey area, in the g , r , and i bands (Hogg et al. 2001; Smith et al. 2002; Ivezić et al. 2004a; Tucker et al. 2006; Padmanabhan et al. 2008). The spectroscopic observations are carried out with a multi-fiber spectrograph between 3800 – 9200 Å, with a resolution of $R \sim 1800 - 2100$ (Blanton et al. 2003). All data have been made publicly available, in periodic data releases (Stoughton et al. 2002; Abazajian et al. 2003, 2004, 2005, 2009; Adelman-McCarthy et al. 2006, 2007, 2008).

The SQLS has been one of the most successful strong lens surveys conducted to date. It identifies lensed quasar candidates among spectroscopically confirmed quasars in the SDSS (Richards et al. 2002; Schneider et al. 2010), by combining two selection algorithms, designed to find both small- and large-separation lenses, respectively. The morphological selection identifies small-separation candidates that are unresolved, yet poorly fitted by the point spread function (PSF); the color selection algorithm searches, in the vicinity of every confirmed quasar, for resolved stellar objects that have similar colors to the quasar. The SQLS has discovered more than 40 new lensed quasars so far (Inada et al. 2012). Together with previously known lenses rediscovered by the SQLS, it has produced a sample of ~ 60 lensed quasars, roughly half of all lensed quasars discovered to date.

SDSS J1320+1644 is a large-separation lensed quasar candidate identified by the color selection algorithm. We reproduce the SDSS multi-band composite image of the system in Figure 1. A faint red object, classified by the automatic pipeline as a galaxy, is detected in between the two blue stellar components constituting the lensed quasar candidate, towards North. We give the SDSS photometric results for the quasars and the red object in Table 1. As a result of the finite size of the optical fibers in the SDSS spectrograph, spectra are usually not obtained for two objects less than $55''$ apart (the "fiber collision"; Blanton et al. 2003), and therefore SDSS spectroscopy is available for only one member of the pair. We

reproduce the spectrum of that object, classified as a quasar at $z = 1.5024 \pm 0.0024$, in Figure 2 (in blue).

3. Follow-up Imaging and Spectroscopy

3.1. Spectroscopy of the quasar pair

Follow-up spectroscopy is necessary to ensure that both stellar components are quasars at the same redshift, in conformity with the gravitational lens or binary quasar hypotheses, as well as to assess their spectral similarities.

The spectroscopy was performed at the Astrophysical Research Consortium Telescope (ARC 3.5 m) located at the Apache Point Observatory. Spectra were taken with the Dual Imaging Spectrograph (DIS³), equipped with a combination of blue and red gratings, B400/R300. The observations were conducted on 2009 February 19 with a 1''5 width slit oriented so that both stellar components are on the slit, with 1500 s exposure and a typical airmass of 1.66. The extracted spectral coverage was 3700 – 10000 Å, with a resolution $R \sim 500$. The data reduction was performed using standard IRAF⁴ tasks.

The spectra shown in Figure 2 (black and red) indicate that both stellar components have similarly shaped quasar broad emission lines (BELs; C III], Mg II) at the same wavelengths, and therefore are quasars at the same redshift. Our redshift estimate based on the C III] and Mg II peaks (including a reanalysis of the original SDSS spectrum, which was taken in a longer, 4200s exposure, and better resolution $R \sim 1850 - 2000$) is 1.487 ± 0.001 , which is slightly lower, and is incompatible with the error bar in the SDSS database. We identify absorption lines in both quasars as the Mg II 2796 Å, 2803 Å doublet and possibly Fe II 2599.4 Å, indicating $z = 0.899$. We identify another Mg II doublet at $z = 1.168$, present only in quasar B (the quasar designation corresponds to that in Figure 4).

The flux ratio A/B increases with wavelength (from ~ 0.8 to ~ 1.5). This could be explained by a combination of microlensing, differential extinction and intrinsic variability, or simply differential slit losses, and does not constitute an argument against the gravitational lensing hypothesis. The flux decrease of quasar A towards shorter wavelengths is also in

³http://www.apo.nmsu.edu/35m_operations/35m_manual/Instruments/DIS/DIS.html

⁴The interactive Reduction and Analysis Facility (IRAF) is distributed by the National Optical Astronomy Observatories, which are operated by the Association of Universities for Research in Astronomy, Inc., under cooperative agreement with the National Science Foundation.

agreement with quasar A having redder colors in the SDSS photometry. We provide a more thorough comparative analysis of the spectra in §6.

Overall, the identical redshift of the two quasars, the similarity of the shapes of the BELs (see Figure 9 for a close-up) as well as the presence of absorption lines at the same redshift, appear consistent with the gravitational lensing hypothesis. Of course, these features are fully consistent with the binary quasar hypothesis as well, in which case spectral differences appear naturally, as there are two distinct quasars.

3.2. UH88 and Subaru Telescope imaging data

Optical follow-up imaging observations were originally conducted with the Tektronix 2048×2048 CCD camera (Tek2k; V , R , I and z bands) and the Wide Field Grism Spectrograph 2 (WFGS2; z band) at the University of Hawaii 2.2-meter (UH88) telescope, in April 2009. The Tek2k camera has a $7'.5 \times 7'.5$ field of view and a pixel scale of $0''.219 \text{ pixel}^{-1}$. The WFGS2 has a $11' \times 11'$ field of view and focal reducer of $0''.34 \text{ pixel}^{-1}$, and was used in imaging mode with the Tek2k camera. Bias and flat frames were also obtained, and the data were reduced using standard IRAF tasks. The standard star system PG0918+029 (Landolt 1992) was observed for photometric calibration, but the zero-points determined from the five individual stars have a scatter of ~ 0.2 mag, likely indicative of non-photometric conditions. In order to obtain a better precision, the instrumental magnitudes of 10 bright stars in the field of view were compared to their SDSS $ugriz$ magnitudes. The Lupton (2005) formulae⁵ were used to transform between $ugriz$ and VRI magnitudes, which resulted in smaller scatter. The exposure time, airmass, seeing, zero-point uncertainty and observation date are given for each band in Table 2.

In the deeper UH88 images (the I and z filters), in addition to the faint photometric object detected between the two quasars in the SDSS data, another object is detected, located almost symmetrically with respect to the quasars (Figure 3). In order to determine the morphological and photometric properties of these two objects, as well as to estimate photometric redshifts, we obtained higher resolution near-infrared (J , H and Ks bands) images with the Multi-Object InfraRed Camera and Spectrograph (MOIRCS; Ichikawa et al. 2006; Suzuki et al. 2008), at the Subaru 8.2-meter telescope (Iye et al. 2004), in April 2010. MOIRCS has two HAWAII-2 2048×2048 detectors providing a $3'.94 \times 6'.90$ total field of view, with a pixel scale of $0''.117 \text{ pixel}^{-1}$. The data (Table 2) were reduced with the MCSRED software package (I. Tanaka et al., in preparation), and the standard star FS33 (Leggett et al.

⁵<http://www.sdss.org/dr5/algorithms/sdssUBVRITransform.html>

2006) was used to estimate the photometric zero points.

In the J , H and Ks imaging (Figure 4), the two faint objects are clearly detected. They have extended morphology and red colors, indicative of fairly high-redshift galaxies. In each band, we modeled all four objects simultaneously using the public software GALFIT (Peng et al. 2002), using nearby bright stars as PSF templates. We fitted the galaxies with a Sérsic profile convolved with the PSF. The resulting astrometry and photometry (including the UH88 photometry) are given in Tables 3 and 4, respectively. We were able to characterize the morphology of the two galaxies, which we summarize in Table 5. The Sérsic index of G1 is close to the canonical value for elliptical galaxies, $n = 4$, whereas for G2 it is close to the typical value for disk galaxies, $n = 1$. We therefore conclude that G1 is an elliptical galaxy, whereas G2 is disk-like. This is also consistent with the bluer color of G2.

We also detected three additional fainter objects in the vicinity of the system. While FWHM measurements and GALFIT modeling are not very reliable, our analysis suggests that the objects are extended, and so we mark them as galaxies G3, G4 and G5 in Figure 4. Aperture photometry, summarized in Table 4, indicates that the colors of G4 (but not of G3 and G5) are very similar to those of G1 and G2, and we therefore assume that this is a galaxy at about the same redshift. We also remark that the $J - H$ colors of G3 and G5 are different from that of A and B, and it is therefore unlikely that these are additional, faint gravitationally lensed quasar images.

In the UH88 and Subaru Telescope imaging observations, the flux ratio of the quasars A and B (A/B) is above unity, in opposition to the SDSS results. The chromatic change in the brightness ranking of the quasar images could be explained by microlensing (see §6.1.2).

4. Photometric redshifts

In order to determine whether the two brighter galaxies are located in the foreground of the quasar pair, as is required by the gravitational lens hypothesis, we need to estimate their redshifts. Although we do not possess spectral data for these galaxies, we can estimate their photometric redshifts, based on their magnitudes in different filters. In order to do so, we use template-fitting estimate methods implemented in the publicly available HyperZ (Bolzonella et al. 2000) and EAzY (Brammer et al. 2008) algorithms. The algorithms fit the observed magnitudes to spectral energy distribution (SED) templates, via χ^2 minimization. As templates, we employ the observed mean SEDs of local galaxies from Coleman et al. (1980, hereafter CWW), which are extrapolated into the ultraviolet and near-infrared with the evolutionary models of Bruzual & Charlot (1993). The EAzY algorithm also uses the

redshift distribution of galaxies of a given apparent magnitude as a Bayesian luminosity prior, following Benitez (2000). This helps to break the degeneracies between multiple probability distribution peaks at different redshifts.

In order to obtain consistent results for the two algorithms, we had to increase the uncertainties on the magnitudes to about double the values quoted in Table 4, which also makes the aperture- and model-determined values consistent. In addition to the statistical errors quoted in that table, additional sources of errors could potentially be introduced by the zero-point uncertainties (Table 2), possible blending of sources due to their close proximity and large seeing, different pixel size in the V , R , I and z band observations (aperture photometry), or the modeling difficulties and PSF uncertainties (model magnitudes).

The results of the photometric redshift estimates are shown in Figure 5 and Table 6. G1 is well-fitted by an elliptical template, and G2 by an Sbc template, consistent with the expectations from the galaxy morphologies (see §3.2). Although the probability distributions are rather broad, they are in agreement, inside the 1σ interval estimated from the redshift probability distributions, with $z = 0.899$, which is the redshift of the absorption lines identified in both spectra. The redshift of the second Mg II absorption system in quasar B, at $z = 1.166$, is rejected at about 2σ confidence level, while the probability of a redshift as high as the quasar redshift appears negligible. Therefore, throughout the rest of this work, we assume that these galaxies are responsible for the absorption lines at $z = 0.899$.

For the faintest objects we detected, G3, G4 and G5, the redshift probability distributions are very broad (Table 6). G3 and G5 show a smaller preferred redshift of $z \sim 0.5$. On the other hand, G4 has a preferred redshift of 1.11, very close to that of the Mg II absorption system at $z = 1.166$. This absorption system is quite strong, with equivalent width $\sim 2.9 \text{ \AA}$ in the rest frame of the absorber. Here the projected proper distance between B and G4 is $21 h_{70}^{-1} \text{ kpc}$ at $z = 1.166$. On the other hand, the Mg II absorption system at $z = 0.899$ has equivalent widths $\sim 2.9 \text{ \AA}$ and $\sim 4.5 \text{ \AA}$ (in the spectra of quasars A and B, respectively) for impact parameter $\sim 35 h_{70}^{-1} \text{ kpc}$, corresponding to the distances between the quasars and G1, G2. Such absorptions at small impact parameters are consistent with the literature (e.g., Churchill et al. 2005, and references therein). The stronger absorption in quasar B could be explained by its closer proximity to one of the galaxies (G1).

5. Gravitational Lens Mass Modeling

5.1. Observational constraints

We next proceed with modeling the system as a gravitational lens. The observational constraints provided by the available astrometry and photometry are the positions of the images A and B, their fluxes (we take the flux ratio to be either $\sim 1.0 \pm 0.2$ or $\sim 1.4 \pm 0.2$, as we will show in §6), and the positions of the two main galaxies expected to act as lenses, G1 and G2. We also know the redshift of the source, $z = 1.487$, and of the lenses, $z = 0.899$. Constraints can also be placed on the "strength" of the lenses, represented by their velocity dispersions, which we infer from the observed luminosities. To this end, we estimate the rest frame R band absolute magnitudes of G1 and G2 as ~ -22.5 and ~ -22.3 , respectively, calculated with HyperZ from the best-fit E and Sbc templates. We use the Faber-Jackson (F-J; Faber & Jackson 1976) and the Tully-Fisher (T-F; Tully & Fisher 1977) laws, with parameters given in Binney & Tremaine (2008), and infer velocity dispersions of 237 ± 54 km s $^{-1}$ and 163 ± 15 km s $^{-1}$, respectively. For G2, which is disk-like, we have assumed a singular isothermal sphere (SIS) profile and estimated the velocity dispersion as $\sigma = v_{\text{circ}}/\sqrt{2}$, where v_{circ} is the circular velocity obtained from the T-F law.

A question worth posing is to what extent must the faintest objects G3, G4 and G5 (assuming the latter two are galaxies), be taken into account when building gravitational lens models. Here we estimate the velocity dispersion of G4, which we have reasons to believe (see §4) is located at $z = 0.899$ or $z = 1.168$, based on its colors, as well as (in the latter case) the existence of strong Mg II absorption features in quasar B, the closest member of the pair. We neglect the contribution of G3 and G5, as they are located further away from images A and B, and are most likely at a significantly different redshift from G1, G2 and G4, based on their colors.

Assuming that G4 is located at the same redshift as G1 and G2 leads to velocity dispersions $\sigma = 150 \pm 35$ km s $^{-1}$ or $\sigma = 105 \pm 10$ km s $^{-1}$, from the F-J and T-F laws, respectively. For $z = 1.168$, these values are $\sigma = 175 \pm 40$ km s $^{-1}$ and $\sigma = 125 \pm 12$ km s $^{-1}$, respectively. However, in this case the galaxy will act as a weaker deflector, as it is located at a different redshift than that of the main deflectors G1 and G2. Assuming that the effect of G4 on the lensing configuration is small (convergence at $z = 1.168$ is $\kappa \sim \theta_{\text{Ein}}/2d \sim 0.028 \pm 0.012$ (F-J) or $\sim 0.014 \pm 0.002$ (T-F), where θ_{Ein} is the Einstein radius of the lens G4 estimated from the velocity dispersion, assuming an SIS profile, and $d = 2''.49$ is the projected angular distance between B and G4), we can treat G4 as an SIS lens situated at $z = 0.899$, but with a smaller effective velocity dispersion. This eliminates the need to introduce multiple lens planes. From Keeton et al. (2003), using κ (convergence) = γ (shear) for the SIS profile,

the effective convergence of G4 at $z = 0.899$ is $\kappa_{\text{eff}} = (1 - \beta)\kappa/(1 - 2\beta\kappa) \sim 0.012 \pm 0.005$ (F-J), or $\sim 0.006 \pm 0.002$ (T-F), where $\beta = D_{12}D_{\text{OS}}/(D_{\text{O2}}D_{\text{1S}})$, $D_{ij} = D(z_i, z_j)$ are angular diameter distances, $z_1 = 0.899$, $z_2 = 1.168$, and O, S refer to the observer and source, respectively. The effective convergence corresponds to an SIS profile at G4 with effective velocity dispersion $\sim 81 \pm 19 \text{ km s}^{-1}$ (F-J) or $\sim 57 \pm 5 \text{ km s}^{-1}$ (T-F). We conclude that, considering all possibilities, an SIS model at $z = 0.899$ for G4 would have a velocity dispersion in the 1σ range of $\sim 118 \pm 66 \text{ km s}^{-1}$.

5.2. Best-fit models

As the number of observational constraints is limited, we focus on simple SIS and NFW lens models and their elliptical counterparts, with or without shear. The singular isothermal profile is known to be a good approximation for the mass distribution in galaxies, based for example on spiral galaxy rotation curves (e.g., Rubin et al. 1978, 1980), measurements from stellar dynamics in elliptical galaxies (e.g., Gerhard & Kronawitter 2001), and gravitational lenses (e.g., Kochanek et al. 1995; Rusin & Kochanek 2005; Koopmans et al. 2009, and references therein). It has also been employed in the lens modeling of galaxy clusters (e.g., Inada et al. 2003). The NFW profile (Navarro et al. 1996), on the other hand, is frequently employed as an approximation of the mass distribution in dark matter haloes, which dominate galaxy clusters.

Based on the velocity dispersion estimate in §5.1, the largest galaxy G1 has an Einstein radius of only $\sim 0''.5 \pm 0''.2$, and an enclosed mass of $\sim (2.1 \pm 1.5) \times 10^{11} h_{70}^{-1} M_{\odot}$. However, the large separation between A and B ($\sim 8''.6$), assuming they are lensed images of a single source, implies an enclosed mass of $\sim 1.2 \times 10^{13} h_{70}^{-1} M_{\odot}$. Consequently, this cannot be a gravitational lens system where the main deflectors are the individual members of a group of galaxies, and we need to invoke a significant embedding dark matter halo.

We subsequently explore models in which the lensing potentials of G1, G2 and G4 are boosted by an embedding dark matter halo. The first model we explore consists of three SIS profiles at the location of the three galaxies, where we initially fix the position of the dark matter halo at the location of G1. We introduce a shear component for G1 (SIS+ γ), and we leave its velocity dispersion as free parameter, so that this model has 14 nominal constraints (quasar image positions (4), fluxes (2), galaxy positions (6) and velocity dispersions (2)), and the same number of nominal parameters (source positions (4) and fluxes (2), lens positions (6), shear and position angle of the main lens (2)). We therefore have 0 degrees of freedom (d.o.f.), and should be able to fit the system perfectly ($\chi^2 \ll 1$), as we in fact do. All gravitational lens modeling is performed with *glafic* (Oguri 2010). We show the critical lines

and caustics for this model in Figure 6 (top left). We report the best fitted parameters of this model (velocity dispersion or mass of the dark matter halo at G1, ellipticity or orientation of shear, position angle, total magnification and time delay), as well as of the subsequent models, in Table 7. We obtained a best fit with a velocity dispersion of $\sim 710 \text{ km s}^{-1}$ for the dark matter halo. We also explored, on a suitable grid, combinations of velocity dispersions for G2 and G4 in the ranges determined in §5.1. We only considered models with $\chi^2 \leq 2.3$, corresponding to the 1σ confidence interval for two parameters. The effect of the range of velocity dispersions is reflected in the range of values for the parameters in Table 7. We tried a similar range of SIS+ γ models at the location of G2, but were unable to produce good fits. We note that G2 is farther away from the line connecting images A and B, and therefore a model centered on G2 is expected to do a poorer job of fitting the data. We do not try to fix the extra SIS profile at the location of G4, as we are not sure whether this galaxy is at the same redshift as G1 and G2 (and therefore part of the same group or cluster), and we would also expect the dark matter halo to be centered closer to the two bright galaxies.

The second model (“SIS free” in Figure 6) is similar to the first, but here we fix the velocity dispersion of G1 as well, and instead we consider an additional, massive SIS component whose position and velocity dispersion are not constrained. This model is most likely a simplification of the real situation, as the simulated dark matter halo is expected to show ellipticity or shear. However, there are not enough observational constraints to uniquely determine those additional parameters. Proceeding as before, we checked different combinations of the velocity dispersions of G1 and G4 (we fixed the velocity dispersion of G2 at the most probable value) and determined the corresponding locations of the massive SIS lens in the lens plane, allowed at 1σ confidence intervals (the black regions in Figure 6, plotted for both possible ranges of intrinsic flux ratios).

For our third model, in addition to modeling the three galaxies with SIS profiles, we fixed an elliptical NFW profile at the location of G1 (Figure 6, bottom left). We parameterize the NFW profile by its virial mass M_{vir} and concentration parameter c_{vir} , and we fix the latter at a fiducial value 6, close to the typical value for galaxy clusters at the mass range and redshift we are interested in (e.g., Binney & Tremaine 2008, and reference therein). We explore different choices of c_{vir} at the end of this section. This model is also successful in reproducing the observables. We are however unable to find a good fit in the case that the NFW profile is fixed at the location of G2.

As a final model (“NFW free” in Figure 6), we use a spherical NFW dark matter halo whose position we leave as a free parameter, in analogy to our second model. Compared to the SIS profile, the NFW profile is shallower at the center, and can therefore produce an additional faint central image. We require that the model produce no more than three images,

and that the central image be ~ 50 times or more fainter than B, which corresponding to our detection limit in the K_s band, which is the deepest, at $S/N \sim 5$. Varying the velocity dispersions of G1 and G4 on a grid, and choosing only those within 1σ confidence interval for two parameters, we also determined the corresponding location of the NFW lens in the lens plane (Figure 6, bottom right, black region). The central image cannot be one of the faint objects G3 or G5, as those objects are too far away from the midpoint between A and B, are also most likely extended, and have different colors.

Our main result in this section is that there is a variety of reasonable mass models that reproduce the observed image configuration. In order for this system to be a two-image gravitationally lensed quasar, we do however require a massive dark matter halo in which the visible galaxies are embedded. This halo should be centered either on G1 (but not on G2) or at some location close to the midpoint between A and B. The choice of the intrinsic flux ratio (either ~ 1.0 or ~ 1.4) does not affect the successful mass models qualitatively. In addition, the velocity dispersions of G1 and G4 can be constrained further, although weakly, in the range determined in §5.1 from their luminosities. These constrained values appear however to be degenerate, and are not relevant in the following discussions. A first caveat is that, when estimating the range of velocity dispersion for each galaxy in §5.1, we have not taken into account the possible evolution of the T-F and F-J with redshift. Although there is no consensus in the literature in this regard (e.g., Böhm et al. (2004) & Fernández Lorenzo (2010) for T-F, Rusin et al. (2003) & Treu et al. (2006) for F-J), the tendency is that galaxies had smaller rotational velocities and velocity dispersions in the past for the same luminosity. This would reduce even more the contribution of the galaxies to the mass models dominated by the dark matter halo. A second caveat applies to G4, in the case that this galaxy is located at $z = 1.166$. In this case, G4 would also be lensed by the dark matter halo at $z = 0.899$, and therefore magnified by a factor $\sim 1.5 - 3$, depending on the assumed lensing model. This would mean that the galaxy is intrinsically fainter, and its contribution to the mass models would be further reduced. We have checked that the best-fit models considered in this section (from which we exclude the contribution of G4) would not produce multiple images of this galaxy.

Finally, we investigate how the choice of the concentration parameter c_{vir} of the NFW profiles affects our results. We explore c_{vir} in the range from 2 to 30, and we optimize all other model parameters. Increasing c_{vir} has the effect of decreasing the total magnification of the images, and increasing the time delay (Table 7). We plot the resulting c_{vir} - virial mass relation in Figure 7. We obtain virtually the same degeneracy for the free NFW profile as for the one fixed at G2. For comparison, we also plot some recently published results on the c_{vir} - virial mass relation: the results of N -body simulations by Duffy et al. (2008), as well as the theoretical and observational results inferred by Oguri et al. (2012a) from

fitting lensing clusters at $z \sim 0.45$. The strong lens selected sample behind the Oguri et al. (2012a) relations is known to be biased towards overestimating the concentrations due to halo triaxiality. If SDSS J1320+1644 is indeed a lens system, it should include the same bias, as it is selected as a strong lens. All these relations are observed to intersect the SDSS J1320+1644 curves in different regions.

6. Quasar Spectro-Photometric Differences

The purpose of this section is to assess the relative contribution of the factors that are responsible for the differences in the available spectroscopic and photometric data of the two quasars, show that these do not discriminate against the gravitational lensing hypothesis, and justify the flux ratio constraint which we have used in §5 for gravitational lens modeling. We base our discussion on the original SDSS spectroscopic data of quasar A and the follow-up spectra of both quasars (Figure 2), as well as all available photometric data, which are summarized in Figure 8.

The three physical phenomena known to modify the spectra of the images of gravitationally lensed quasars are differential extinction due to dust in the lensing galaxy (e.g., Falco et al. 1999), microlensing due to stars in the lens (e.g., Chang & Refsdal 1979; Schneider et al. 2006), and intrinsic quasar variability coupled with the time delays between images. The first process is a static one, whereas the other two are time-dependent. We assess their effects on the continuum, broad-band fluxes and BELs in turn.

6.1. Continuum emission and broad-band fluxes

6.1.1. Differential extinction

The first difference we notice in the follow-up spectra of quasars A and B is the gradual drop in the flux ratio A/B with wavelength, shortward of about 7000 Å. Such an effect has previously been observed in several lensed quasars, such as SDSS J1001+5027 (Oguri et al. 2005) and SDSS J1313+5151 (Ofek et al. 2007). Differential extinction (reddening) between the quasar images could explain this effect, as it is most effective at short wavelengths. Here we caution however that the monotonous drop in the flux ratio may also be due to unknown differential slit losses in the ARC 3.5 m spectroscopy. Nonetheless the effect must be real at least in part, because the flux drop is supported by the available photometry from u to z band, which shows quasar A to be redder than B (see also Figures 1 and 8). In addition, the flux ratios inferred from the UH88 photometry, obtained just two months after the follow-up

spectra, are broadly consistent with the spectral ratios at the respective wavelengths. On the other hand, extinction should be insignificant in the longest wavelength filter K_s , which corresponds roughly to J band in the rest frame of G1 and G2. A caveat however is that there is no obvious galaxy responsible for the extinction in A, i.e. located much closer to A than the other galaxies are to B. In the binary quasar hypothesis, internal differential extinction in the unrelated quasar host galaxies would be a natural explanation.

In contrast, the large change in the spectral slope of quasar A at short wavelengths, on a time span of 13 months, between the original SDSS and ARC observations, requires a significant contribution of the time-dependent phenomena. While the slope change can also be caused by slit losses, the two sets of photometric data in the $V - z$ band range, taken ~ 4 years apart, also shows the brightness rank of the two quasars interchanging, with A getting brighter, and B becoming fainter. Therefore time-dependent phenomena must be acting on the quasars. We next look into the extent to which microlensing can explain these data.

6.1.2. Microlensing

Microlensing by stars in the lens can cause significant magnification/demagnification only if the source has structure on the scale of the Einstein radius of the microlens projected into the source plane, $\lesssim R_{\text{Ein,S}}$ (e.g., Schneider et al. 1992), where (following Richards et al. (2004) in the next equations)

$$R_{\text{Ein,S}} = \sqrt{\frac{4GM}{c^2} \frac{D_{\text{OS}} D_{\text{LS}}}{D_{\text{OL}}}} \sim 4.0 \left(\frac{M}{0.1 M_{\odot}} \right)^{1/2} h_{70}^{-1/2} \text{ lt-days}, \quad (1)$$

and D_{OL} , D_{OS} and D_{LS} are the angular diameter distances to the lens, the source, and between the lens and source, respectively.

The two physical regions of a quasar which are of relevance here are the accretion disk responsible for the continuum emission, and the BEL region. The accretion disk has an extent of a few light-days or less (e.g., Morgan et al. 2008) in the rest frame ultraviolet, corresponding to the optical region of the observed spectrum of SDSS J1320+1644. On the other hand, the BEL region is as large as a few light-weeks or light-months (e.g., Clavel et al. 1991), with lower ionization lines originating at larger distances. Thus, we expect that the structures prone to microlensing, in the order of decreasing likelihood, are the continuum, the C III] BEL, and the Mg II BEL.

Assuming that the microlensing variability is due to the motion of stars in the lensing galaxies, which we consider to be dominated by the proper motion of the galaxies (with

transverse velocity v_{\perp}), there are two timescales to the microlensing event. The first timescale is the expected duration of the event, which is the time in which the microlens crosses the source, $t_{\text{src}} \sim 2R_{\text{src}}/v_{\text{eff}}$. Here $v_{\text{eff}} = v_{\perp}/(1+z_l) D_{\text{OS}}/D_{\text{OL}}$ is the effective transverse velocity projected into the source plane, but expressed as a distance over the observed-frame time. Using $v_{\perp} \sim \sigma$, where σ is the velocity dispersion in the galaxy group/cluster, results in

$$t_{\text{src}} \sim 4.1 \left(\frac{R_{\text{src}}}{1 \text{ lt-day}} \right) \left(\frac{v_{\perp}}{700 \text{ km s}^{-1}} \right)^{-1} \text{ yr.} \quad (2)$$

The second timescale is the mean interval between microlensing events, which is crudely estimated as the time needed to cross an Einstein radius,

$$t_{\text{Ein}} \sim R_{\text{Ein,S}}/v_{\text{eff}} \sim 8.2 \left(\frac{M}{0.1 M_{\odot}} \right)^{1/2} \left(\frac{v_{\perp}}{700 \text{ km s}^{-1}} \right)^{-1} h_{70}^{1/2} \text{ yr.} \quad (3)$$

Although these results are rough estimates, they are close to the timescales on which our data shows spectral and photometric variations. More careful analytical considerations of the expected microlensing light curves (e.g., Yonehara et al. 2008) as well as ray-shooting techniques to account for the fact that the source could be microlensed by an ensemble of stars at any particular time (e.g., Kayser et al. 1986) show that microlensing can indeed cause variations in amplitude comparable to, or even larger than we observe. In addition, in standard accretion disk theory (e.g., Peterson 1997), short wavelength emission originates at comparatively smaller distances from the central engine, and so is preferentially affected by microlensing. This is in agreement with the large changes we detect at progressively shorter wavelengths in our two-epoch spectra of quasar A. Conversely, since the near-infrared emission is expected to originate at larger distances from the center than the UV or optical continuum, we expect the longest wavelength band Ks (originating approximately at z band in the quasar rest frame) to be less affected by microlensing.

One possible argument against microlensing could be that, since the two galaxies are fairly distant in projection from the quasar pair ($\sim 35 h_{70}^{-1}$ kpc), there may be no stars to account for microlensing. We note that evidence of microlensing has previously been found in both SDSS J1004+4112 (e.g., Richards et al. 2004), and SDSS J1029+2623 (e.g., Oguri et al. 2008b), the two large-separation cluster lenses; in those cases however, the galaxies believed to host the stars responsible for microlensing are located at slightly smaller projected separations of $\lesssim 20 - 30 h_{70}^{-1}$ kpc from the quasar images.

6.1.3. Intrinsic variability

We now turn our attention to the extent that the observed spectrophotometric changes in quasar A (for which the slopes of the continuum as a function of wavelength, at two different epochs, bracket those of quasar B) can originate from intrinsic quasar variability. This is estimated from the structure function (e.g., Yonehara et al. 2008, and reference therein)

$$V = (1 + 0.024M_i) \left(\frac{\Delta t_{\text{RF}}}{\lambda_{\text{RF}}} \right)^{0.3} \text{ mag}, \quad (4)$$

which predicts the magnitude change for a quasar of i band absolute magnitude M_i , at a given rest frame wavelength λ_{RF} in units of \AA , for a rest frame time interval between observations of Δt_{RF} (in days). The structure function has been measured from a quasar sample with $M_i \sim -21$ to ~ -30 (Vanden Berk et al. 2004), in the rest frame optical/UV, and on a rest frame time range of up to 2 years. We also note that the characteristic time scale for optical variability of quasars is of the order 1 year (Ivezić et al. 2004b), which is comparable with the time delays in the source rest frame (0.4 - 2.8 years) that we obtain between the images, in our best lensing models.

In practice, we use the structure function to check if it can reproduce spectral changes in quasar A of a factor of ~ 2 in flux (~ 0.75 mag), at $\sim 4500 \text{ \AA}$ ($\sim 1800 \text{ \AA}$ rest frame), in the 13 months (~ 160 days rest frame) between the original SDSS and the follow-up spectroscopy. Using the image magnifications we obtain from the lensing models (Table 7), and the fact that the source rest frame i band corresponds to the observed $H - Ks$ bands, we estimate the source quasar absolute brightness to be $M_i \sim -22.0$ to ~ -25.7 . Since the structure function is larger for fainter quasars, we use the former value and obtain an upper estimate of $\Delta m \sim 0.23$ (because this is a magnitude difference, it has the same value in the rest frame as in the magnified, observed-frame). This value is too small to explain the spectral changes at short wavelengths. We note however that the structure function might be able to explain the flux changes of ~ 0.3 mag ($\Delta m = 0.25$) in both quasars in the z band, in ~ 4 years, and it may also introduce flux variations of about 0.26 - 0.23 mag at the observed-frame $J - Ks$ bands, during the maximum rest frame time interval of the quasar sample, ~ 2 years. We must however point out two factors that weaken our result: 1) that slit losses may be responsible in part for the spectral changes at short wavelengths, and 2) that the structure function is a statistical average over a sample of quasars, therefore brightness changes of larger amplitude are not ruled out in individual objects (magnitude differences larger than 0.75 occur in about 1% of quasars; Vanden Berk et al. (2004)).

6.1.4. Summary and remarks

Our analysis shows that the spectral shapes of A & B (in the continua) are compatible with the gravitational lensing hypothesis, where the differences are caused by differential extinction, microlensing and intrinsic variability. Microlensing and extinction are more important at short wavelengths than intrinsic variability, and slit losses may also explain the change in the spectrum of A. Regarding the intrinsic flux ratio, all three spectral flux ratios of the two quasars, which we plotted in Figure 2, are fairly constant in the range 7200 – 8400 Å (if we ignore the atmospheric absorption lines in the follow-up spectra), with $A(\text{SDSS})/A$ (the original SDSS spectrum of A divided by the follow-up spectrum of A) fairly close to 1, and A/B , $A(\text{SDSS})/B \sim 1.4$. This latter value is in excellent agreement with the flux ratio we measure in the J , H and Ks bands, where we expect differential extinction and microlensing to be weakest. Together, these results suggest that the intrinsic flux ratio, which would ideally be measured in the far-infrared or radio, is $\sim 1.4 \pm 0.2$, and all three flux-altering physical factors considered are weak in the 7200 – 8400 Å spectral range. Here we chose the error bar on the flux ratio somewhat arbitrarily, slightly larger than the scatter in the flux ratio at 7200 – 8400 Å as well as the J , H and Ks bands. We further discuss the intrinsic flux ratio based on the study of the BELs in the next section.

We also remark that the two quasars were detected in the mid-infrared by WISE (Wright et al. 2010), at almost the same epoch as the Subaru MOIRCS J , H and Ks observations. The flux ratio at 3.4, 4.6 and 12 μm is ~ 1 (Table 8), but we consider this to be broadly consistent with the value above, because the quasars were detected at quite low S/N $\sim 10 - 20$, and the fluxes were measured by deblended profile fits, at very poor angular resolution ($6''.1$, $6''.4$, $6''.5$ and $12''.0$ in the four bands, respectively). There is also the possibility of unknown flux contamination from the two bright galaxies. The quasar pair also appears to be radio quiet, based on non-detection in the Faint Images of the Radio Sky at Twenty-cm survey, which is sensitive to > 1 mJy/beam. Radio detection could have provided a test against the lensing hypothesis (if only one quasar was radio loud), as well as provide accurate image fluxes for use in the lensing models (in case both quasars were radio loud), due to insensitivity to differential extinction and microlensing.

6.2. Broad emission lines

Since microlensing is expected to affect the continuum and BELs differently, we look for consequences of this effect in the observed spectra. We find that the spectral flux ratio A/B of the two images (Figure 2) shows a decrease at the center of the Mg II BEL, compared to

the surrounding continuum⁶, but no detectable change at the location of the C III]. Since the flux ratios contain contributions from the BELs as well as the continuum, we subtract the continuum component in order to study the BELs. We estimate the BEL flux with three different methods: 1) we fit the continuum (while avoiding regions with emission lines) with a 5th order polynomial, which we subtract; 2) we connect with straight lines the continuum level on both sides of each BEL, and integrate the flux above these lines; 3) we proceed as in 1), then we use a window of width 100 Å, centered on the peak of the BELs, and we consider only the flux inside, in order to avoid errors in the flux estimate of the BEL wings. When calculating the flux ratios A(SDSS)/A and A(SDSS)/B for the Mg II BEL using the first two methods, we corrected for the telluric absorption affecting the blue wing, by extrapolating over it. We report the results in Table 9, where the errors reflect the range in the results of the three methods. We also plot these results on top of the flux ratios in Figure 2.

Our result is that the three flux ratios in the emission lines (A(SDSS)/A, A(SDSS)/B and A/B) are all consistent with ~ 1 for Mg II, but show scatter in the case of C III]. In concordance with our discussion in §6.1.2, we interpret these fluxes to mean that the Mg II BEL is not affected by microlensing. In principle there are two ways in which to piece together the results obtained so far.

- We could assume that the intrinsic flux ratio is $\sim 1.4 \pm 0.2$, as seen in the previous section. As the observed continuum ratios are $A/B \sim 1.4$ and $A(\text{SDSS})/A \sim 1$ in the neighborhood of Mg II, there is only little room for microlensing in the continuum. However A/B and $A(\text{SDSS})/B$ are both ~ 1 in the Mg II line, which suggests extinction in image A, at this location in the spectrum, of about 0.2 - 0.5 mag; here we accounted for the uncertainty in the flux ratio. Contribution from intrinsic variability at the BEL (which should follow variability in the continuum in a matter of weeks to months), as well as possibly small microlensing in the continuum, would reduce and possibly eliminate the need for extinction, while also being natural ways of affecting the continuum and BEL differentially.

- On the other hand, the intrinsic flux ratio may be $\sim 1.0 \pm 0.2$, assuming that the Mg II BEL flux ratio is affected by neither microlensing nor extinction. Here we assumed error bars slightly larger than those in Table 9, to allow for intrinsic variability. This requires that the flux ratio of ~ 1.4 in the continuum, found in the data redward of the Mg II BEL, is due to microlensing. This assumption is still in agreement with the results in §6.1.2, and in particular Equation 2, which is an order-of-magnitude estimate. In this interpretation, the flux change at long wavelengths occurs on timescales larger than those sampled by

⁶This does not refer to the increase in A(SDSS)/B and A(SDSS)/A at the blue wing of the Mg II BEL, which is due to telluric absorption calibrated out in the SDSS spectrum, but not in the follow-up spectra.

our observations, whereas those at shorter wavelengths are noticeable. This assumption is testable via deep, high resolution mid-infrared observations, as the mid-infrared emitting region is expected to be too large for microlensing to occur. In this regard, the flux ratio is in excellent agreement with the WISE data at 3.4, 4.6 and 12 μm , where we nonetheless believe the errors to be underestimated (see §6.1.3). This interpretation would also explain why the flux ratio decreases slightly with increasing wavelength between the H and Ks bands, reaching unity in the WISE bands.

Concerning the C III] BEL, the fact that the spectral flux ratios at the location of C III] (the contribution from the continuum combined with the BEL) are different from those of the continuum-subtracted, BEL-only emission (for which $A(\text{SDSS})/A \neq 1$ and $A(\text{SDSS})/B \neq A/B$), could mean that the C III] emission is affected by microlensing, yet not in a manner that is identical to the neighboring continuum. However the fact that, compared to the Mg II BEL, we do not detect outstanding changes in the (continuum combined with the BEL) flux ratios as we move from the surrounding continuum to the BEL, would mean that the differences between the microlensing in the continuum and the C III] BEL cannot be large. These results are insensitive to effects from possible slit losses, as these should affect the continuum and the BEL in the same way. We note that, although we find microlensing in the C III] BEL but not the Mg II BEL, there are cases in the literature where microlensing has been found in both lines (e.g., Sluse et al. 2007, 2011). Although here we assumed the lensing hypothesis and interpreted all C III] flux differences in terms of microlensing, in the binary quasar hypothesis the difference between the overall and the BEL-only $A(\text{SDSS})/A$ flux must be attributed to intrinsic variability.

We also attempted an independent spectral analysis by applying the macro-micro spectral decomposition technique of Sluse et al. (2011) to the follow-up spectra of A and B. This results in an inferred intrinsic flux ratio of ~ 0.9 , derived for the Mg II line, and a relative microlensing ratio of ~ 1.4 between A and B, in the adjacent continuum. It also supports our conclusion that the C III] line is more microlensed than the Mg II line. This analysis implies that intrinsic variability and/or differential extinction (which may also affect the values above) are required in order to prevent the estimated microlensing from being stronger in the red than in the blue continuum.

Lastly, we plot the continuum subtracted BELs in Figure 9. The overall shapes appear very similar, in concordance with the gravitational lensing hypothesis. However the blue wing of C III] appears more shallow in quasar A. This could be due to microlensing changing the shape of the BEL (e.g., Richards et al. 2004), as well as intrinsic variability.

7. Additional considerations

7.1. Environment of the lens

Since our attempts to model the system as a two-image gravitationally lensed quasar require a significant additional dark matter component, we next look at the environment of the lens, in order to search for clues to the existence of a possible galaxy cluster.

We proceed by making color-magnitude and color-color diagrams of the galaxies in the MOIRCS field of view ($\sim 1900 \times 1660 h_{70}^{-1}$ kpc at $z = 0.899$, centered on SDSS J1320+1644), using the J , H and Ks bands. We aim to isolate the galaxies that are similar in color to G1 and G2, and study their spatial distribution around the target. We use SExtractor (Bertin & Arnouts 1996) to catalogue and match all the objects in the field of view, and we isolate the galaxies by requiring the SExtractor stellarity parameter to be less than 0.2 in all three bands. We eliminate a few galaxies that are very close together, so that aperture photometry would fail, which leads to a sample of 98 galaxies.

From Table 4, using the aperture photometry, we determine the colors ($J - H$, $H - Ks$) = $(0.87 \pm 0.07, 0.88 \pm 0.05)$ for G1, and $(0.87 \pm 0.08, 0.80 \pm 0.05)$ for G2. We notice small differences in the aperture photometry with the same radius, computed by SExtractor (MAG_APERT), but they are too small to be of consequence in the resulting color-magnitude (Figure 10) and color-color diagram (Figure 11, left). The color-magnitude diagrams show one branch with small scatter in $J - H$, on which G1 and G2 lie, but larger scatter in $H - Ks$. In color-color space, G1 and G2 lie close to each other, and close to the concentration at $(J - H, H - Ks) \sim (0.9, 0.7)$. Thus there may be an excess of galaxies at the redshift of G1 and G2, indicative of a cluster.

We attempt a color cut at $0.8 < J - H < 1.1$ and $0.6 < H - Ks < 0.9$, which includes the concentration of galaxies as well as G1 and G2. In Figure 11 (right), we plot the positions of the galaxies selected by this color-cut from the MOIRCS field of view centered on SDSS J1320+1644; they seem to spatially surround the target. We caution however that the broad color cut may contain galaxies at different redshift. A multidimensional color plot would help break the degeneracies, but the UH88 bands, even the deep z band, detect only a few of the galaxies visible in the MOIRCS bands and do not allow a systematic treatment.

Our analysis therefore hints that G1 and G2 are embedded at the center of a galaxy cluster, which in turn supports the existence of a heavy dark matter halo associated with the cluster, required by our models in §5.2. We next provide an estimate of the content of dark matter.

7.2. Mass-to-light ratios

We compute the mass-to-light (M/L) ratio by assuming that SDSS J1320+1644 is a lensed system, and compare it with the M/L ratio of the other lenses discovered by the SMLS⁷ (Inada et al. 2012). We fit each lens with an SIS profile, in which case the Einstein radius θ_E is simply half the image separation. For the quasars with more than two images, we consider θ_E to be half the largest separation between the images. The mass inside the Einstein radius is simply determined as

$$M(\leq \theta_E) = \frac{D_{\text{OL}}D_{\text{OS}}}{D_{\text{LS}}} \frac{c^2\theta_E^2}{4G} \simeq 1.23 \times 10^8 h_{70}^{-1} M_{\odot} \left(\frac{D_{\text{OL}}D_{\text{OS}}/D_{\text{LS}}}{1 h_{70}^{-1} \text{ Mpc}} \right) \left(\frac{\theta_E}{1 \text{ arcsec}} \right)^2. \quad (5)$$

To determine the luminosity of the lenses, we referred to the discovery papers (Inada et al. 2012, and references therein) and estimated the rest frame R band magnitudes of all the galaxies with available photometry, located between the images, using the HyperZ algorithm. To convert the rest frame magnitudes into fluxes we used $M_R = 4.48 - 2.5 \log L/L_{\odot,R}$, where $M_{\odot,R} = 4.48$ is the R band magnitude of the Sun. The M/L ratios were computed in terms of the solar M/L ratio, $\Upsilon_{\odot} = 1 M_{\odot}/L_{\odot}$.

We attached no error bars to the results of these rough calculations. Not accounting for the effects of lens ellipticity and external shear for each (mostly double-image) system should introduce an error of $\sim 10\%$ on the masses (Rusin & Kochanek 2005). Also, the redshifts of several lenses are not accurately known, which influences both the masses and the inferred luminosities. Photometry for most lenses is only available in three bands (we eliminate 10 objects for which the lens is detected in only one band), and their morphology is typically unknown. It is therefore difficult to choose the appropriate CWW spectral template for calculating the rest frame R band luminosity. However we know that the majority of lens galaxies are ellipticals, as these have larger velocity dispersions (Turner et al. 1984), and so we generally assume the elliptical template, unless the lens is known to be a spiral, or the fit of another template is much better. Also, luminosities should be more accurate for lenses at $z \sim 0.2 - 0.3$, because at this redshift the rest frame R band is redshifted into the observed-frame I band, where observations are usually available. For SDSS J1320+1644, the lens redshift estimate means that the rest frame R band is redshifted into the J band, where we have photometry.

The results of our M/L estimates are shown in Figure 12, in which we plot the mass-to-

⁷<http://www-utap.phys.s.u-tokyo.ac.jp/~sdss/smls/lens.html>

light ratios against the reduced image separations. The reduced image separation $\Delta\theta_{\text{red}} \equiv \Delta\theta D_{\text{OS}}/D_{\text{LS}}$ scales out the dependence on the source and lens distance, thus representing a physical property of the lensing object.

The image separation is the most important observable, because it reflects the depth of the gravitational potential of the lensing object and therefore the structure responsible for the lensing phenomenon. In order of increasing image separation, the nature of the lens can be a galaxy, a group of galaxies, or a cluster of galaxies. Since clusters are dominated by dark matter much more than normal galaxies, we expect that, as the image separation increases from the galaxy lens to the cluster lens range, so does the M/L ratio. This is in fact the result we obtain in Figure 12 for the SQLS lens sample, which shows a positive correlation between the image separation and M/L. Most small-separation lenses at $\Delta\theta \sim 1''$ are clustered at $M/L \sim 1 - 10 \Upsilon_{\odot}$, consistent with the estimates from the dynamics of elliptical galaxies and their stellar populations (Padmanabhan et al. 2004), whereas the two known cluster-scale lenses (SDSS J1004+4112 and SDSS J1029+2623) both have a larger M/L. We obtain a similarly large M/L for SDSS J1320+1644.

7.3. X-ray emission constraints

In Section §5.2, we concluded that in the gravitational lensing hypothesis, SDSS J1320+1644 requires a dark matter halo with mass or velocity dispersion typical of galaxy groups or clusters. In such deep gravitational potential wells, the intra-cluster gas is heated into a hot diffuse plasma, becoming an X-ray emitter, typically via thermal bremsstrahlung (free-free emission; Felten et al. 1966) and recombination (free-bound emission) processes. A detection or non-detection of X-ray emission could therefore potentially prove or disprove the lensing hypothesis, serving as a proxy for the existence of a dark matter halo.

SDSS J1320+1644 has no detected X-ray emission in ROSAT, the deepest all-sky X-ray survey conducted to date. For comparison, the two largest-separation lensed quasars SDSS J1004+4112 and SDSS J1029+2623, as well as Q0957+561 (with an image separation smaller than SDSS J1320+1644), all show X-ray emission that is detected with ROSAT. A consideration of whether the lack of X-ray detection is enough to disprove the lensing hypothesis is therefore necessary.

A simple estimate of the gas temperature expected in an SIS potential with velocity dispersion $\sim 700 \text{ km s}^{-1}$ is $T = \mu m_p \sigma^2 / k \sim 3.6 \times 10^7 \text{ K}$ ($kT = 3.15 \text{ keV}$), where we have employed standard notation, and $\mu \sim 0.6$ (solar abundance). At $kT \gtrsim 2.5 \text{ keV}$, the predominant X-ray emission process is thermal bremsstrahlung (e.g., Gitti et al. 2011), and

therefore we consider the total power per unit volume emitted by thermal bremsstrahlung,

$$J(T) = 1.4 \times 10^{-27} n_e n_i T^{1/2} Z^2 \bar{g}(T) \quad (\text{erg s}^{-1} \text{ cm}^{-3}), \quad (6)$$

which is accurate to within 20% for Gaunt factor $\bar{g}(T) = 1.2$ (Rybicki & Lightman 1979); here n_e and n_i are the electron and ion density, respectively, and we assume $Z = 1$. We assume that the plasma covers the spherical volume inside the quasar pair, $V = 4\pi(D_{\text{OL}}\Delta\theta/2)^3/3 \simeq 4.8 \times 10^{69} \text{ cm}^3$; here $\Delta\theta$ is the separation between the quasar pair. The expected flux on the ROSAT detector is therefore $J(T)V/[4\pi D_{\text{OL}}^2(1+z)^4] \simeq 1.1 \times 10^{-11} n_e n_i \text{ erg s}^{-1} \text{ cm}^{-2}$. Since for ROSAT the detection limit for a mean 400 s exposure is 1 cnt $(400 \text{ s})^{-1} \simeq 2.2 \times 10^{-14} \text{ erg s}^{-1} \text{ cm}^{-2}$ (Gregorio-Hetem et al. 2009), and typical electron density values in clusters are $10^{-1} - 10^{-5} \text{ cm}^{-3}$ (Chièze et al. 1998), we would expect a number of counts in the range $10^{-7} - 10 (400 \text{ s})^{-1}$ (assuming $n_e = n_i$). However, there is no reason to assume that the dark matter halo is spatially limited to the region between the quasars. In fact, for concentration parameters $c_{\text{vir}} < 10$, the virial radius of the NFW profile is larger than $\sim 2'$, such that it extends to the possible galaxy cluster we detect around the system. In this case the expected number of counts increases by $\sim (2'/8'6)^3$, to $10^{-4} - 10^4 (400 \text{ s})^{-1}$. We conclude that the lensing cluster would not be detected by ROSAT if the gas density is at the low end of plausible values. The non-detection of an X-ray signal therefore cannot be used as a sufficient argument against gravitational lensing. For comparison, SDSS J1004+4112, SDSS J1029+2623 and Q0957+561 are detected at 16, 94 and 53 cnt $(400 \text{ s})^{-1}$, respectively. A similar calculation would find roughly similar expected number of counts for these objects, where the main uncertainty comes from the density and spatial extent of the emitting plasma.

8. Summary, discussion and conclusions

We have reported the discovery as part of the SQLS of SDSS J1320+1644, a pair of quasars at $z = 1.487$ with two galaxies in between, in a cross-like configuration. We have estimated the redshift of the two galaxies as $z = 0.899$, based on absorption lines observed in the quasar spectra and consistency with the photometric redshifts of the galaxies.

We used the observational constraints to investigate whether the system is a two-image gravitationally lensed quasar or a binary quasar. We showed that the key to differentiate between the gravitational lens and binary pair hypotheses is whether or not there exists a dark matter halo at the location of the system, capable of boosting the gravitational potential of the galaxies. We estimated the required virial mass or velocity dispersion of this

halo, as well as the expected time delays and image magnifications, using a variety of SIS and NFW profiles. We were also able to show that the halo can only be centered on the brighter, elliptical galaxy, or somewhere in between the two quasars (but not on the disk-like galaxy), as well as to set constraints on the velocity dispersions of these two galaxies, and an additional, fainter third galaxy. The third galaxy may be located at either $z = 0.899$ or $z = 1.168$. In the first case, it would further support the existence of a halo indicative of a galaxy group or cluster, and in the second it would explain the presence of a strong absorption system in one of the quasars.

We have found a substantial number of galaxies in the field, surrounding the quasar pair, with colors consistent with $z = 0.899$ (based however on only three filters). If this is a galaxy cluster, the quasar pair would reside behind the center of the cluster potential, which would provide the required dark matter halo lens. The calculated mass-to-light ratio assuming the lensing hypothesis is in agreement with what would be expected from a cluster-scale lens.

We have performed a comparative analysis of the spectra of the two quasars (as well as determined the intrinsic flux ratio of the two quasars), and concluded that all observed differences can be attributed to a combination of extinction, microlensing and intrinsic variability, in support of the gravitational lensing hypothesis.

The most similar known system to our target is arguably Q0957+561 (Walsh et al. 1979), which has two quasar images separated by $6''.17$ and one lensing galaxy that is part of a confirmed cluster that boosts the image separation. That system shows, in addition, evidence of strongly lensed arcs, which are the extended images of the lensed quasar host galaxy (Bernstein et al. 1993).

We conclude that SDSS J1320+1644 is a probable gravitationally lensed quasar, although we are unable to prove this beyond, doubt based on our available data. We propose the following observations as a means of establishing the true nature of this object unambiguously:

- Monitoring of the quasar fluxes to look for correlated variations (a time delay) supporting the lensing hypothesis. Although we do not possess sufficient constraints to estimate a robust time delay, our best estimates are $\sim 1 - 7$ years, based on our lensing models.
- Spectroscopy of the two brightest galaxies would determine if they are indeed at the same redshift, consistent with the spectral absorption lines, as assumed in our galaxy cluster hypothesis. These galaxies are faint in the V , R , I , z and SDSS bands, and therefore the photometric redshifts are fairly uncertain. Multi-object spectroscopy would provide a means to check the redshift of the surrounding galaxies, and therefore either consistently prove or disprove the cluster hypothesis. At the very least, deeper imaging in other bands is required

to constrain the photometric redshift of the surrounding galaxies.

- Deep X-ray observations would provide an independent measure of the velocity dispersion of intracluster gas at the location of the two galaxies, and test the presence of the embedding dark matter halo.

- Deep, wide field optical imaging of the region could be used to detect weak lensing associated with the possible lensing cluster.

- As the most time-effective way of testing the lensing hypothesis, we suggest deep adaptive optics or Hubble Space Telescope observations to study the morphology of the quasar host galaxies, and look for extended arc-like features, characteristic of gravitational lensing. We note that there is a 16.6 mag (R band) star $\sim 58''$ from the target, which could be used as a tip-tilt star for the Laser Guide Star Adaptive Optics capabilities of Subaru Telescope.

Should this system indeed prove to be a gravitational lens, it would be the third-largest separation gravitationally lensed quasar in the SQLS, and the largest separation two-image lensed quasar known. These large separation lenses are important to include in a complete statistical sample such as the one provided by the SQLS (Inada et al. 2012), in order to constrain the hierarchical structure formation at cluster mass scales. They are also exceedingly rare, because the probability of quasars strongly lensed by clusters is 1-2 orders of magnitudes smaller than that of quasars lensed by galaxies (e.g., Inada et al. 2012).

This work was supported in part by the FIRST program "Subaru Measurements of Images and Redshifts (SuMIRe)", World Premier International Research Center Initiative (WPI Initiative), MEXT, Japan, and Grant-in-Aid 23740161 for Scientific Research from the Japan Society for the Promotion of Science (JSPS).

C.E.R. and I.K. acknowledge the support of the JSPS Research Fellowship. D.S. acknowledges supports from Deutsche Forschungsgemeinschaft, reference SL172/1-1. M.A.S acknowledges support from NSF grant AST-0707266. The authors recognize and acknowledge the very significant cultural role and reverence that the summit of Mauna Kea has always had within the indigenous Hawaiian community. We are most fortunate to have the opportunity to conduct observations from this superb mountain.

This publication makes use of data products from the Wide-field Infrared Survey Explorer, which is a joint project of the University of California, Los Angeles, and the Jet Propulsion Laboratory/California Institute of Technology, funded by the National Aeronautics and Space Administration.

Funding for the SDSS and SDSS-II has been provided by the Alfred P. Sloan Foundation,

the Participating Institutions, the National Science Foundation, the U.S. Department of Energy, the National Aeronautics and Space Administration, the Japanese Monbukagakusho, the Max Planck Society, and the Higher Education Funding Council for England. The SDSS Web Site is <http://www.sdss.org/>.

The SDSS is managed by the Astrophysical Research Consortium for the Participating Institutions. The Participating Institutions are the American Museum of Natural History, Astrophysical Institute Potsdam, University of Basel, Cambridge University, Case Western Reserve University, University of Chicago, Drexel University, Fermilab, the Institute for Advanced Study, the Japan Participation Group, Johns Hopkins University, the Joint Institute for Nuclear Astrophysics, the Kavli Institute for Particle Astrophysics and Cosmology, the Korean Scientist Group, the Chinese Academy of Sciences (LAMOST), Los Alamos National Laboratory, the Max-Planck-Institute for Astronomy (MPIA), the Max-Planck-Institute for Astrophysics (MPA), New Mexico State University, Ohio State University, University of Pittsburgh, University of Portsmouth, Princeton University, the United States Naval Observatory, and the University of Washington.

REFERENCES

- Abazajian, K., et al. 2003, *AJ*, 126, 2081
- Abazajian, K., et al. 2004, *AJ*, 128, 502
- Abazajian, K., et al. 2005, *AJ*, 129, 1755
- Abazajian, K. N., et al. 2009, *ApJS*, 182, 543
- Adelman-McCarthy, J. K., et al. 2006, *ApJS*, 162, 38
- Adelman-McCarthy, J. K., et al. 2007, *ApJS*, 172, 634
- Adelman-McCarthy, J. K., et al. 2008, *ApJS*, 175, 297
- Auger, M. W., Treu, T., Bolton, A. S., Gavazzi, R., Koopmans, L., V, E., Marshall, P. J., Bundy, K., Moustakas, L. A. 2009, *ApJ*, 705, 1099
- Benitez, N. 2000, *ApJ*, 536, 571
- Bernstein, G. M., Tyson, J. A. & Kochanek, C. S. 1993, *ApJ*, 105, 816
- Bertin, E., & Arnouts, S. 1996, *AAPS*, 117, 393

- Binney, J., & Tremaine, S. 2008, *Galactic Dynamics: Second Edition*, ed. Binney, J. & Tremaine, S. (Princeton University Press)
- Böhm, A., et al. 2004 *A&A*, 420, 97
- Bolzonella, M., Miralles, J.-M., & Pelló, R. 2000, *A&A*, 363, 476
- Blanton, M. R., Lin, H., Lupton, R. H., Maley, F. M., Young, N., Zehavi, I., & Loveday, J. 2003, *AJ*, 125, 2276
- Brammer, G. B., van Dokkum, P. G., & Coppi, P. 2008, *ApJ*, 686, 1503
- Bruzual A., G., & Charlot, S. 1993, *ApJ*, 405, 538
- Chang, K., & Refsdal, S. 1979, *Nature*, 282, 561
- Chièze, J.-P., Alimi, J.-M., & Teyssier, R., 1998, *ApJ*, 495, 630
- Churchill, C. W., Kacprzak, G. G., Steidel, C. C. 2005, in *Proceedings IAU Colloquium No. 199, Mg II absorption through intermediate redshift galaxies*
- Claeskens, J.-F., & Surdej, J. 2002, *A&AR*, 10, 263
- Clavel, J. et al. 1991, *ApJ*, 366, 64
- Coleman, G. D., Wu, C.-C., & Weedman, D. W. 1980, *ApJS*, 43, 393
- Cutri, R. M., et al. 2012, *Explanatory Supplement to the WISE All-Sky Data Release Products*, http://www.apo.nmsu.edu/35m_operations/35m_manual/Instruments/DIS/DIS.html
- Decarli, R., Treves, A., & Falomo, R. 2009, *MNRAS*, 396, L31
- Djorgovski, S. 1991, in Crampton D., ed., *ASP Conf. Ser. Vol. 21, The Space Distribution of Quasars*. Astron. Soc. Pac., San Francisco, p. 349
- Doi, M., et al. 2010, *AJ*, 139, 1628
- Duffy, A. R., Schaye, J., Kay, T. J., Dalla Vecchia, C. 2008, *MNRAS*, 390, L64
- Faber, S. M., & Jackson, R. E. 1976, *ApJ*, 204, 668
- Falco, E. E., et al. 1999, *ApJ*, 523, 617
- Faure, C., et al. 2008, *ApJS*, 176, 19

- Felten, J. E., Gould, R. J., Stein, W. A., & Woolf, N. J. 1966, *ApJ*, 146, 955
- Férrnandez Lorenzo, M., Cepa, J., Bongiovanni, A., Pérez García, A. M., Lara-López, M. A., Popović, M., & Sánchez-Portal, M. 2010, *A&A*, 521, 27
- Fukugita, M., Ichikawa, T., Gunn, J. E., Doi, M., Shimasaku, K., & Schneider, D. P. 1996, *AJ*, 111, 1748
- Gerhard, O. & Kronawitter, A. 2001, *AJ*, 121, 1936
- Gitti, M., Brighenti, F., McNamara, B. R. 2012, *AdAst*, 2012, 1
- Green, P. J., Myers, A. D., Barkhouse, W., A., Mulchaey, J. S., Bennert, V. N., Cox, T., J., Aldcroft, T., L. 2010, *ApJ*, 710, 1578
- Gregorio-Hetem, J., Montmerle, T., Rodrigues, C. V., Marciotto, E., Preibisch, T., Zinnecker, H. 2009, *A&A*, 506, 711
- Gunn, J. E., et al. 1998, *AJ*, 116, 3040
- Gunn, J. E., et al. 2006, *AJ*, 131, 2332
- Hennawi, J. F. et al. 2006, *AJ*, 131, 1
- Hewett, P. C., Foltz, C. B. & Harding, M. E., 2005, *AJ*, 115, 383
- Hogg, D. W., Finkbeiner, D. P., Schlegel, D. J., & Gunn, J. E. 2001, *AJ*, 122, 2129
- Hopkins, P. F., Hernquist, L., Cox, T. J., Di Matteo, T., Martini, P., Robertson, B., Springel, V., *ApJ*, 630, 705
- Hopkins, P. F., Hernquist, L., Cox, T. J., Di Matteo, T., Robertson, B., Springel, V., *ApJS*, 163, 1
- Hopkins, P. F., Bundy, K., Hernquist, L., Ellis, R. S., *ApJ*, 659, 976
- Hopkins, K., Hernquist, Cox, T. J., Kereš, D., *ApJS*, 175, 356
- Ichikawa, T., et al. 2006, *Proc. SPIE*, 6269, 38
- Impey, C. D., Petry, C. E., Foltz, C. B., Hewett, P. C., & Chaffee, F. H. 2002, *ApJ*, 574, 623
- Inada, N., et al. 2003, *Nature*, 426, 810
- Inada, N., et al. 2005, *PASJ*, 57, L7

- Inada, N., et al. 2006, ApJ, 653, L97
- Inada, N., et al. 2008, AJ, 135, 496
- Inada, N., et al. 2010, AJ, 140, 403
- Inada, N., et al. 2012, AJ, 143, 119
- Ivezić, Ž., et al. 2004a, *Astronomische Nachrichten*, 325, 583
- Ivezić, Ž., Lupton, R. H., Juric, M., et al. 2004b, in *IAU Symp. 222, The Interplay among Black Holes, Stars and ISM in Galactic Nuclei*, ed. Th. Storchi Bergmann, L.C. Ho & H.R. Schmitt (Cambridge: Cambridge Univ. Press), 525
- Iye, M., et al. 2004, PASJ, 56, 381
- Kayo, I., Oguri, M. 2012, in print. (arXiv:1203.6410v1)
- Kayser, R., Refsdal, S., & Stabell, R. 1986, A&A, 166, 36
- Keeton, C. R., Christlein, D., & Zabludoff, A. I. 2000, ApJ, 545, 129
- Keeton, C. R. 2003, ApJ, 584, 664
- Kochanek, C. S. 1995, ApJ, 445, 559
- Kochanek, C. S., Falco, E. E., & Muñoz, J. A. 1999, ApJ, 510, 590
- Koopmans, L. V. E., et al. A&A, 2000, 361, 815
- Koopmans, L. V. E., et al. 2009, ApJ, 703, L51
- Landolt, A. U. 1992, AJ, 104, 340
- Leggett, S. K., et al. 2006, MNRAS, 373, 781
- Lupton, R., Blanton, M. R., Fekete, G., Hogg, D. W., O’Mullane, W., Szalay, A., Wherry, N. 2004, PASP, 116, 133
- McLure, R. J., Dunlop, J., S. 2004, MNRAS, 352, 1390
- More, A., Cabanac, R., More, S., Alard, C., Limousin, M, Kneib, J. P., Gavazzi, R., Motta, V. 2012, ApJ, 749, 38
- Morgan, C. W., Eyler, M. E., Kochanek C. S., Morgan, N. D., Falco, E. E., Vuissoz, C., Courbin, F., Meylan, G. 1992, ApJ, 676, 80

- Mortlock, D. J., Webster, R. L., & Francis, P. J. 1999, MNRAS, 309, 836
- Navarro, J. F., Frenk, C., S., White, S. D. M. 1996, ApJ, 462, 563
- Ofek, E. O., Oguri, M., Jackson, N., Inada, N., Kayo, I. 2007, MNRAS, 382, 412
- Oguri, M., et al. 2004, ApJ, 605, 78
- Oguri, M., et al. 2005, ApJ, 622, 106
- Oguri, M., et al. 2006, AJ, 132, 999
- Oguri, M. 2006, MNRAS, 367, 1241
- Oguri, M., et al. 2008a, AJ, 135, 512
- Oguri, M., et al. 2008b, ApJ, 676, L1
- Oguri, M. 2010, PASJ, 62, 1017
- Oguri, M., et al. 2012a, MNRAS, 420, 3213
- Oguri, M., et al. 2012b, AJ, 143, 120
- Padmanabhan, N., et al. 2004, New Astronomy, 9, 329
- Padmanabhan, N., et al. 2008, ApJ, 674, 1217
- Peng, C. Y., Ho, L. C., Impey, C. D., & Rix, H.-W. 2002, AJ, 124, 266
- Peterson, B. M., 1997, An introduction to active galactic nuclei, Cambridge University Press
- Pier, J. R., Munn, J. A., Hindsley, R. B., Hennessy, G. S., Kent, S. M., Lupton, R. H., & Ivezić, Ž. 2003, AJ, 125, 1559
- Richards, G. T., et al. 2002, AJ, 123, 2945
- Richards, G. T., et al. 2004, AJ, 610, 679
- Rubin, V. C., Kent Ford, W. Jr., Thonnard, N. 1978, ApJ, 225, L107
- Rubin, V. C., Kent Ford, W. Jr., Thonnard, N. 1980, ApJ, 238, 471
- Rusin, D., et al. 2003, ApJ, 587, 143
- Rusin, D., Kochanek, C. S. 2003, ApJ, 623, 666

- Rybicki, G. B., & Lightman, A. P., 1979, *Radiative Processes in Astrophysics*, Wiley-VCH
- Schlegel, D. J., Finkbeiner, D. P., & Davis, M. 1998, *ApJ*, 500, 525
- Schneider, P., Ehlers, J., & Falco, E. E. 1992, *Gravitational Lenses*, Springer-Verlag (Berlin Heidelberg New York)
- Schneider, P., Kochanek, C., & Wambsganss, J. 2006, *Gravitational Lensing: Strong, Weak and Micro*, Saas-Fee Advanced Course 33, Springer
- Schneider, D. P., et al. 2010, *AJ*, 139, 2360
- Sluse, D., Claeskens, J. F., Hutsemékers, D., Surdej, J. 2007, *A&A*, 468, 885S
- Sluse, D., et al. 2011, *A&A*, 528, 100S
- Smith, J. A., et al. 2002, *AJ*, 123, 2121
- Stoughton, C., et al. 2002, *AJ*, 123, 485
- Suzuki, R., et al. 2008, *PASJ*, 60, 1347
- Treu, T, Koopmans, L. V., Bolton, A., S., Burles, S., Moustakas, & L. A. 1984, *ApJ*, 640, 662
- Tucker, D. L., et al. 2006, *Astronomische Nachrichten*, 327, 821
- Tully, R. B., Ostriker, J. P., & Fisher, J. R. 1977, *A&A*, 54, 661
- Turner, E. L., Ostriker, J. P., & Gott, J. R. 1984, *ApJ*, 284, 1
- Vanden Berk, A., et al. 2004, *ApJ*, 601, 692
- Vilenkin, A. 1984, *ApJ*, 282, L51
- Walsh, D., Carswell, R. F., & Weymann, R. J. 1979, *Nature*, 279, 381
- Weedman, D. W., Weymann, R. J., Green, R. F., & Heckman, T. M. 1982, *ApJ*, 255, L5
- Wright, E. L., et al. 2010, *AJ*, 140, 1868
- Wucknitz, O., Wisotzki, L., Lopez, S., & Gregg, M. D. 2004, *A&A*, 405, 445
- Yonehara, A., Hirashita, H., Richter, P. 2008, *A&A*, 478, 95
- York, D. G., et al. 2000, *AJ*, 120, 1579

Table 1. Original SDSS photometry

Object & designation	<i>u</i>	<i>g</i>	<i>r</i>	<i>i</i>	<i>z</i>
SDSS J132059.17+164402.59 (A)	20.16±0.04	19.58±0.02	19.16±0.02	18.88±0.02	18.86±0.04
	20.10±0.06	19.54±0.02	19.17±0.02	18.84±0.02	18.84±0.06
SDSS J132059.73+164405.6 (B)	18.93±0.02	18.84±0.02	18.74±0.02	18.62±0.02	18.67±0.03
	18.91±0.02	18.78±0.01	18.74±0.02	18.57±0.02	18.69±0.06
SDSS J132059.37+164406.66 (G2)	25.05±0.79	24.13±0.36	23.01±0.22	22.10±0.17	21.77±0.47
	24.53±2.84	23.99±0.58	23.08±0.41	21.96±0.27	21.60±0.80

Note. — The AB magnitudes are corrected for Galactic extinction following Schlegel et al. (1998). The object designations are those from §3.2. The first line for each object gives the PSF magnitudes (A, B), or best model magnitudes (G2), and the second line gives aperture photometry magnitudes. Objects G3 and G5 (see Figure 4) were also identified as photometric targets by the SDSS pipeline, but their magnitudes are not reproduced, as they are considered unreliable.

Table 2. Summary of follow-up imaging observations

Filter	Instrument	Exposure	Airmass	Seeing	Zero-point uncertainty	Observation date
<i>V</i>	UH88/Tek2k	3×100 s	1.20	1.0 – 1.2	0.10	2009 April 15
<i>R</i>	UH88/Tek2k	4×100 s	1.40	1.0 – 1.2	0.08	2009 April 15
<i>I</i>	UH88/Tek2k	7×100 s	1.20	1.0 – 1.2	0.07	2009 April 15
<i>z</i>	UH88/Tek2k	8×100 s	1.20	1.0 – 1.2	0.07	2009 April 15
<i>z</i>	UH88/WFGS2	24×180 s	1.14 – 1.53	1.0 – 1.2	0.04	2009 April 17
<i>J</i>	Subaru/MOIRCS	4×150 s	1.03	0.4	0.01	2010 April 2
<i>H</i>	Subaru/MOIRCS	4×120 s	1.05	0.4	0.01	2010 April 2
<i>Ks</i>	Subaru/MOIRCS	4×150 s	1.09	0.4	0.01	2010 April 2

Note. — Zero-point uncertainties in the *V*, *R*, *I* and *z* filters include the scatter between the values obtained from the 10 stars used in the estimation, as well as the Lupton (2005) transformations. In the *J*, *H* and *Ks* filters, the uncertainties include those quoted in the catalogue and the aperture photometry errors. There the actual error may be ~ 0.05 mag, if the differences between catalogues and the values obtained from different frames of the standard star are included. Among the two *z* band observations, only the deeper one is considered throughout this article.

Table 3. Astrometry results for SDSS J1320+1644

Object	Δx [arcsec]	Δy [arcsec]
A	0.000 ± 0.002	0.000 ± 0.002
B	-8.066 ± 0.002	2.939 ± 0.002
G1	-4.991 ± 0.006	0.117 ± 0.006
G2	-2.960 ± 0.006	3.843 ± 0.007
G4	-9.169 ± 0.019	5.173 ± 0.024
G3	-1.682 ± 0.018	-5.166 ± 0.022
G5	-12.177 ± 0.021	7.176 ± 0.020

Note. — Astrometry of the SDSS J1320+1644 system, determined in the MOIRCS Ks band (the Sérsic index of the galaxies has been left unconstrained in the GALFIT modeling). The positive directions of x and y are defined towards West and North, respectively. The quoted errors are the GALFIT statistical errors (A, B, G1, G2), and those determined with the IRAF PHOT task (G3, G4, G5).



Fig. 1.— SDSS *gri* color-composite (Lupton et al. 2004) centered on the SDSS J1320+1644 pair, obtained on 2005, June 6. The image scale is $50'' \times 50''$. North is up and East is to the left. The exposure was 54 s in each band and the SDSS pixel scale is $0''.396$. The two quasars are the blue objects near the center.

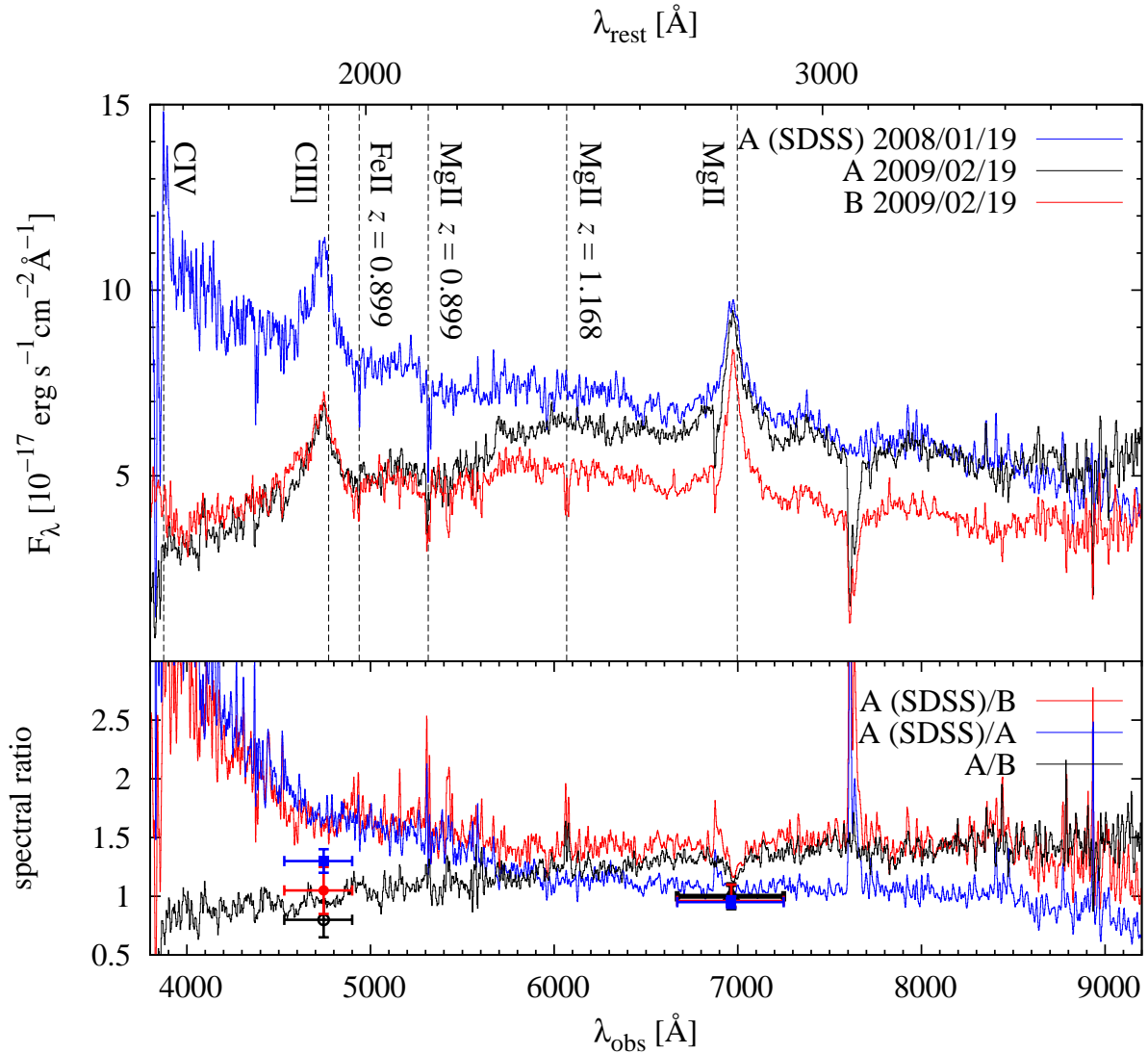


Fig. 2.— *Top*: Spectra of the two stellar components (quasars) in SDSS J1320+1644, A and B. For component A, we plot the original SDSS spectrum (blue), as well as the ARC 3.5 m follow-up spectrum (black). The quasar designation corresponds to Figure 4 (object A is the component to the South-West, in Figure 1). The emission and absorption lines we identified are marked. Two absorption systems in the follow-up spectra, at the blue wing of Mg II and at $\sim 7600 \text{ \AA}$, are due to atmospheric absorption (these have been calibrated out of the original SDSS spectrum). *Bottom*: the ratio of all three spectral pairs, as well as the flux ratios corresponding to the continuum-subtracted broad emission lines (BELs), following Table 9. Here the horizontal error bars mark the wavelength region spanned by the BELs.

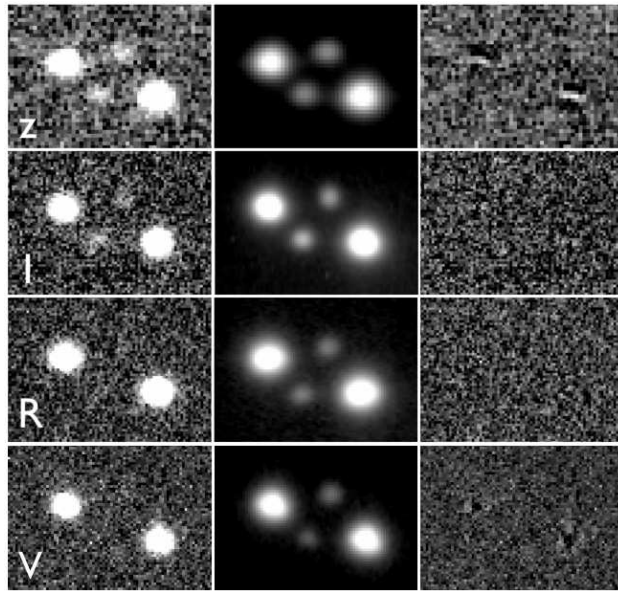


Fig. 3.— Imaging of SDSS J1320+1644 with the UH88 telescope. In each of the V , R , I and z bands, the images to the left show the original observations, the ones in the center show the best models obtained with GALFIT, and those to the right show the residuals after subtracting the fitted models. The snapshots are $11''.8 \times 16''.6$. North is up and East is to the left.

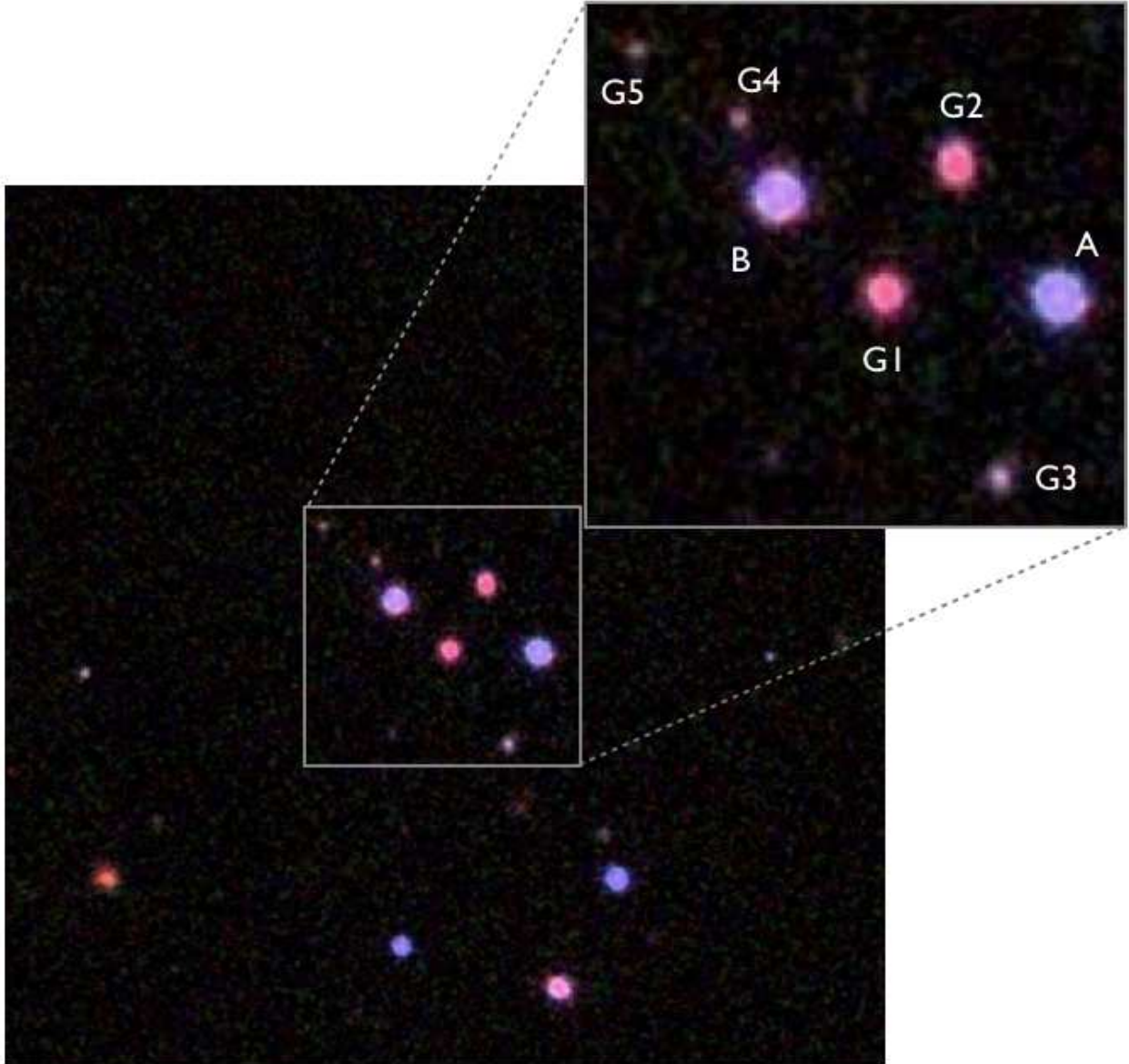


Fig. 4.— Subaru Telescope imaging of SDSS J1320+1644. The image scale (without the close-up) and orientation correspond to Figure 1. This is a small fraction of the MOIRCS field of view centered on SDSS J1320+1644 (see the panel to the right in Figure 11). The image is a color-composite of the J , H and K_s frames, using the algorithm of Lupton et al. (2004).

Table 4. Follow-up photometry of the SDSS J1320+1644 system

Object	V	R	I	z	J	H	K_s
A	19.23 ± 0.01	18.68 ± 0.01	18.33 ± 0.01	18.62 ± 0.01	17.62 ± 0.01	16.82 ± 0.01	16.67 ± 0.01
	19.20 ± 0.01	18.71 ± 0.01	18.31 ± 0.01	18.71 ± 0.01	17.62 ± 0.02	16.86 ± 0.01	16.67 ± 0.01
B	19.30 ± 0.01	18.92 ± 0.01	18.67 ± 0.01	19.00 ± 0.01	18.06 ± 0.01	17.29 ± 0.01	17.02 ± 0.01
	19.28 ± 0.01	18.94 ± 0.01	18.66 ± 0.01	19.10 ± 0.02	18.04 ± 0.02	17.29 ± 0.02	16.98 ± 0.02
G1	23.63 ± 0.37	23.01 ± 0.22	21.66 ± 0.11	21.62 ± 0.10	20.04 ± 0.02	18.83 ± 0.12	18.22 ± 0.02
	23.02 ± 0.23	22.85 ± 0.16	21.47 ± 0.09	21.83 ± 0.12	20.00 ± 0.06	19.13 ± 0.04	18.25 ± 0.03
G2	23.16 ± 0.24	23.04 ± 0.22	22.12 ± 0.16	21.51 ± 0.08	20.22 ± 0.02	19.28 ± 0.02	18.53 ± 0.02
	23.25 ± 0.28	23.52 ± 0.29	22.52 ± 0.23	21.65 ± 0.10	20.20 ± 0.06	19.33 ± 0.05	18.54 ± 0.04
G3					21.42 ± 0.12	20.24 ± 0.10	20.07 ± 0.10
G4					21.86 ± 0.14	21.05 ± 0.14	20.35 ± 0.10
G5					22.23 ± 0.17	21.08 ± 0.14	20.80 ± 0.13

Note. — The values are in magnitudes (all in the Vega system, except for the z band, in the AB system). For A, B, G1 and G2, the first line indicates model magnitudes provided by GALFIT (morphological fit), and the second line aperture photometry obtained with the IRAF PHOT task. For G3, G4 and G5, only aperture photometry results are given. Galactic extinction (Schlegel et al. 1998) and atmospheric extinction have been corrected. Quoted errors are statistical errors only. Errors do not include uncertainties in the photometric zero-points (Table 2), in the PSF or due to the galaxy modeling parameters. Aperture photometry has been measured in all bands with a fixed $\sim 3''.1$ diameter aperture ($\sim 1''.9$ for G4 and G5), selected to maximize the amount of light from the target, as well as minimize contamination from the other objects. In the V , R , I and z bands, contamination may be higher due to the larger seeing. In order for the models to converge, the morphological parameters of the Sérsic profiles fitted to these four bands were constrained to the values determined in the K_s band (i.e., Sérsic index fixed to the closest canonical value of 1 or 4, effective radius).

Table 5. Morphological parameters of the two bright galaxies

Object	Effective radius [arcsec]	Sérsic index	Axis ratio (b/a)	Position angle [deg]
G1	0.21 ± 0.01	3.19 ± 0.48	0.63 ± 0.04	-3.9 ± 3.9
G2	0.36 ± 0.01	0.43 ± 0.07	0.67 ± 0.02	0.9 ± 3.1

Note. — Morphological parameters are fitted by GALFIT in the Ks band, with attached statistical errors. The position angle is measured from North towards East.

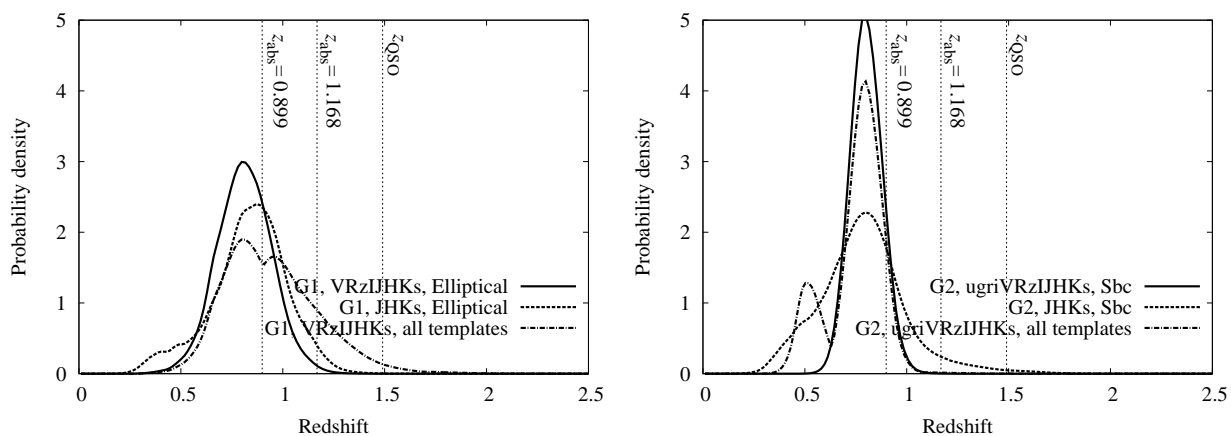


Fig. 5.— Photometric redshift probability distributions, normalized to unit area, for the two galaxies G1 (*left*) and G2 (*right*). The probability distributions are calculated with EAzY using the magnitudes in Tables 1 and 4 (see also §4 for details) for the elliptical template, Sbc template, or marginalized over all spectral templates. The redshift of the quasar pair, as well as those of the absorption line systems identified in the quasar spectra, are marked with vertical lines.

Table 6. Best-fit photometric redshifts

Object & template	Used filters z	Best-fit z	1σ limits	2σ limits	$\chi^2/\text{d.o.f.}$ (d.o.f.)
G1, E (EAzY)	VRIzJHKs	0.81	0.67 – 0.96	0.53 – 1.10	0.34 (6)
G1, E (HyperZ)	VRIzJHKs	0.89	0.76 – 0.95	0.70 – 1.00	0.67 (6)
G1, E (EAzY)	JHKs	0.83	0.65 – 1.02	0.38 – 1.20	0.42 (2)
G1, E (HyperZ)	JHKs	0.92	0.84 – 1.00	0.76 – 1.06	0.09 (2)
G2, Sbc (EAzY)	<i>ugri</i> VRIzJHKs	0.80	0.71 – 0.89	0.64 – 0.97	0.46 (10)
G2, Sbc (HyperZ)	<i>ugri</i> VRIzJHKs	0.88	0.81 – 0.92	0.61 – 0.96	1.93 (10)
G2, Sbc (EAzY)	JHKs	0.79	0.57 – 0.97	0.38 – 1.32	0.29 (2)
G4, all (EAzY)	JHKs	1.11	0.56 – 1.58	0.29 – 1.98	0.05 (2)
G3, all (EAzY)	JHKs	0.55	0.47 – 1.10	0.27 – 1.55	2.07 (2)
G5, all (EAzY)	JHKs	0.60	0.52 – 1.45	0.30 – 1.94	0.84 (2)

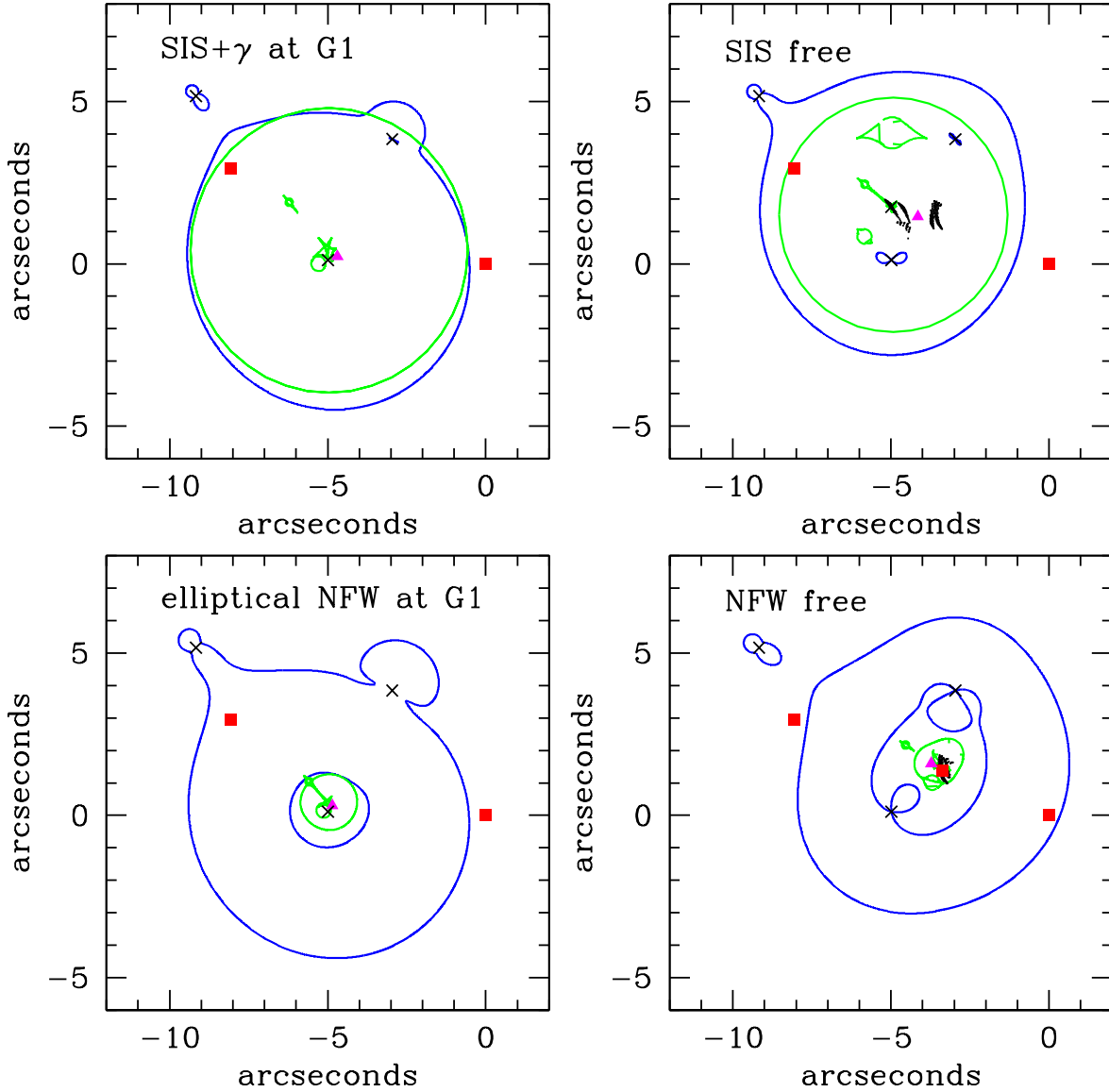


Fig. 6.— Gravitational lensing models. *Top left:* A and B are two images of a source lensed primarily by a large velocity dispersion SIS (with shear) profile centered on G1; *top right:* same as previous, but the position of the primary SIS (without shear) lens is not fixed; *bottom left:* A and B are two images of a source lensed primarily by a large elliptical NFW profile centered on G1; *bottom right:* same as previous, but the position of the spherical NFW lens is not fixed. Critical lines and caustics are drawn in blue and green, respectively, with the velocity dispersions of G1, G2 and G4 fixed at their most probable values (237, 163 and 118 km s^{-1} , respectively), unless the adopted model requires otherwise. Only NFW profiles with $c_{\text{vir}} = 6$ are drawn. Symbols denote image, source and lens positions (red squares, magenta triangles and black crosses, respectively). The black regions close to the center of the large caustic of the free position models show the locations of this primary lens, as the velocity dispersions of G1, G2 and G4 are varied over the allowed 1σ range ($\chi^2 \leq 2.3$).

Table 7. Parameters of the best-fit lensing models

model	σ [km s ⁻¹] or M [$h_{70}^{-1}M_{\odot}$]	e or γ	θ_e or θ_{γ} [deg]	μ_{tot}	Δt [days]
SIS+ γ at G1	710 ± 8 km s ⁻¹	0.026 ± 0.011	20 ± 20	18 ± 2	911 ± 21
SIS free	645 ± 25 km s ⁻¹	-	-	37 ± 29	-860 ± 460 / 1630 ± 940
elliptical NFW at G1	$(5.5 \pm 0.5) \times 10^{13} h_{70}^{-1}M_{\odot}$ ($c_{\text{vir}} = 30$)	0.03 ± 0.01	20 ± 13	13.5 ± 0.5	1095 ± 15
	$(4.2 \pm 0.7) \times 10^{14} h_{70}^{-1}M_{\odot}$ ($c_{\text{vir}} = 6$)	0.018 ± 0.012	-	60 ± 12	510 ± 40
	$(3.15 \pm 0.35) \times 10^{15} h_{70}^{-1}M_{\odot}$ ($c_{\text{vir}} = 2$)	0.01 ± 0.01	-	147 ± 43	320 ± 41
NFW free	$(4.9 \pm 0.4) \times 10^{13} h_{70}^{-1}M_{\odot}$ ($c_{\text{vir}} = 30$)	-	-	41 ± 18	-638 ± 262
	$(4.0 \pm 0.4) \times 10^{14} h_{70}^{-1}M_{\odot}$ ($c_{\text{vir}} = 6$)	-	-	99 ± 46	-547 ± 223
	$(3.2 \pm 0.1) \times 10^{15} h_{70}^{-1}M_{\odot}$ ($c_{\text{vir}} = 2$)	-	-	175 ± 75	-380 ± 80

Note. — The range on each parameter is obtained by changing the velocity dispersions of G1, G2 and G4 over the allowed 1σ range (see §5). e and γ are the ellipticity and shear, respectively, and θ_e , θ_{γ} are the respective position angles (measured East of North). μ_{tot} is the total magnification of images A and B, and the predicted time delay Δt is positive if image A leads.

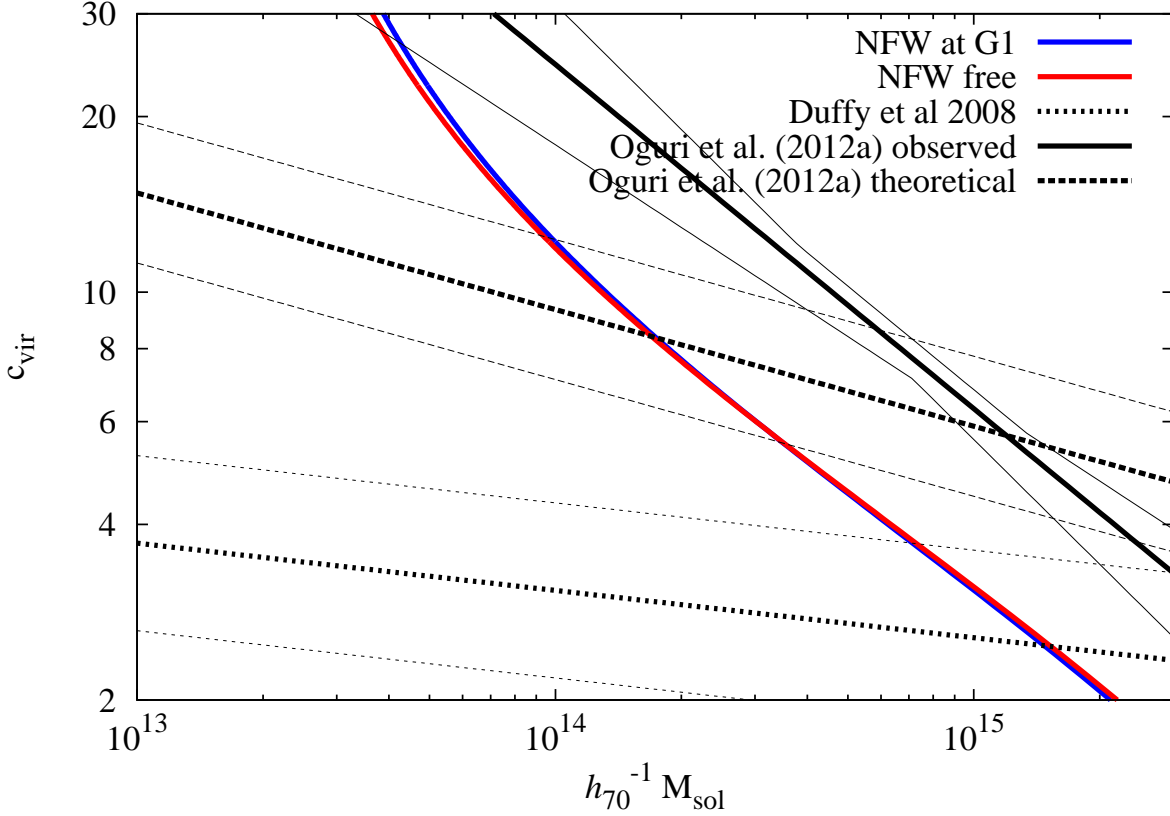


Fig. 7.— The c_{vir} - virial mass degeneracy of the NFW profiles. The thick black lines show published relations from both simulations and observations, while the thin lines show the corresponding 1σ ranges. A caveat is that the Oguri et al. (2012a) theoretical curve has been derived for a cluster redshift $z = 0.45$, which corresponds to the mean redshift of their observed cluster sample. The blue and red curves show the results of these work, for the NFW profile fixed at G1, as well as with unconstrained (free) location, respectively.

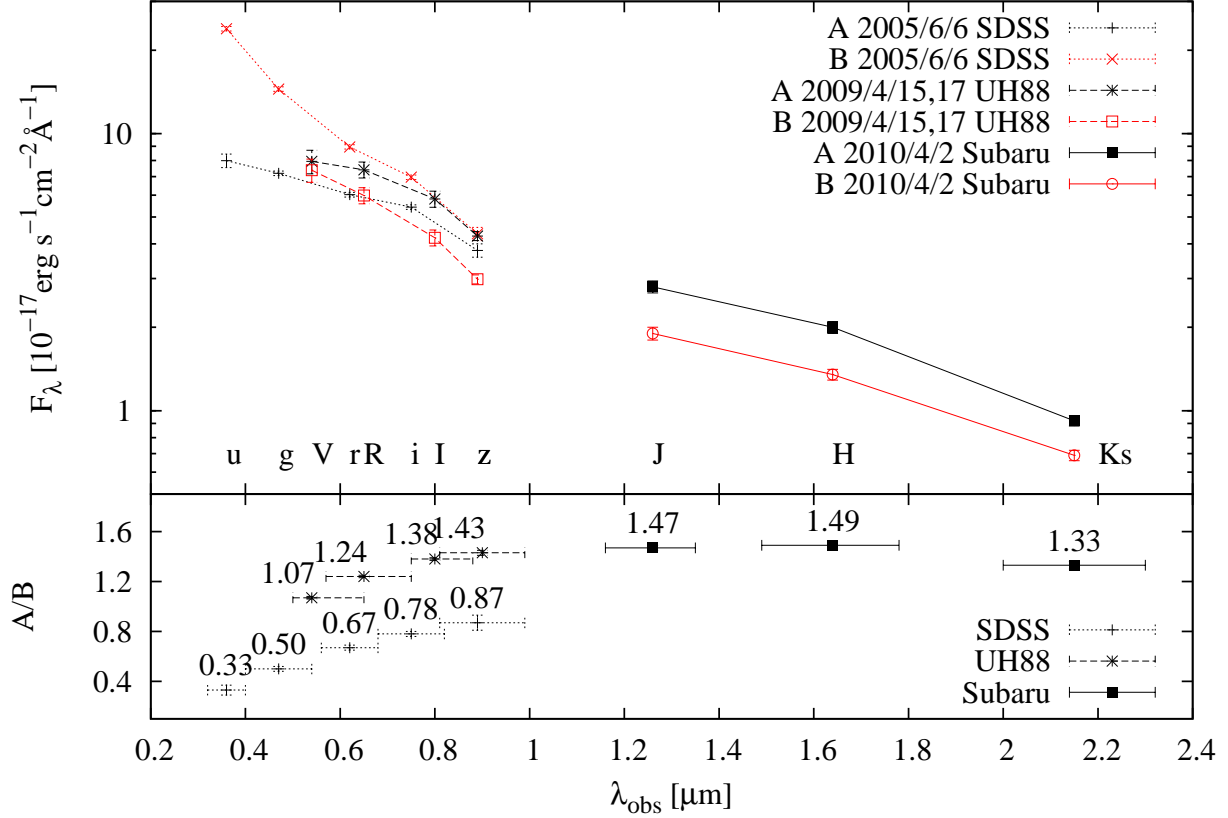


Fig. 8.— Broadband photometric flux and flux ratios of quasars A and B, determined from the aperture photometry in Tables 1 and 4, which include curve of growth corrections. The photometric bands are marked, and the horizontal bars of the flux ratios indicate the width of the filters. We use the photometric errors corresponding to the zero-point uncertainties, from Table 2. The WISE mid-infrared data from Table 8, which is considered less reliable (see §6.1.3), is not plotted.

Table 8. WISE mid-infrared photometry of the SDSS J1320+1644 quasar pair

Object & flux ratio	W1 (3.4 μm)	W2 (4.6 μm)	W3 (12 μm)	W4 (22 μm)
A	15.32 ± 0.05	13.99 ± 0.05	10.92 ± 0.10	9.06 ± 0.53
B	15.32 ± 0.05	14.04 ± 0.05	10.85 ± 0.09	7.97 ± 0.20
A/B	1.00 ± 0.07	1.05 ± 0.07	0.94 ± 0.12	0.53 ± 0.19

Note. — The deblended profile-fit magnitudes are in the Vega system. The observations were performed between 2010, January 7 and 2010, June 30. The values in W4 are particularly unreliable, as the quasars are detected at $S/N \sim 2 - 5$, with an angular resolution of $12''$, larger than the quasar separation.

Table 9. Emission-line spectral flux ratios after continuum-subtraction.

Ratio	C III]	Mg II
A(SDSS)/B	1.05 ± 0.2	0.95 ± 0.05
A/B	0.8 ± 0.15	1.0 ± 0.1
A(SDSS)/A	1.3 ± 0.1	0.95 ± 0.05

Note. — The uncertainties correspond to the range in the three different types of measurement (see §6.2).

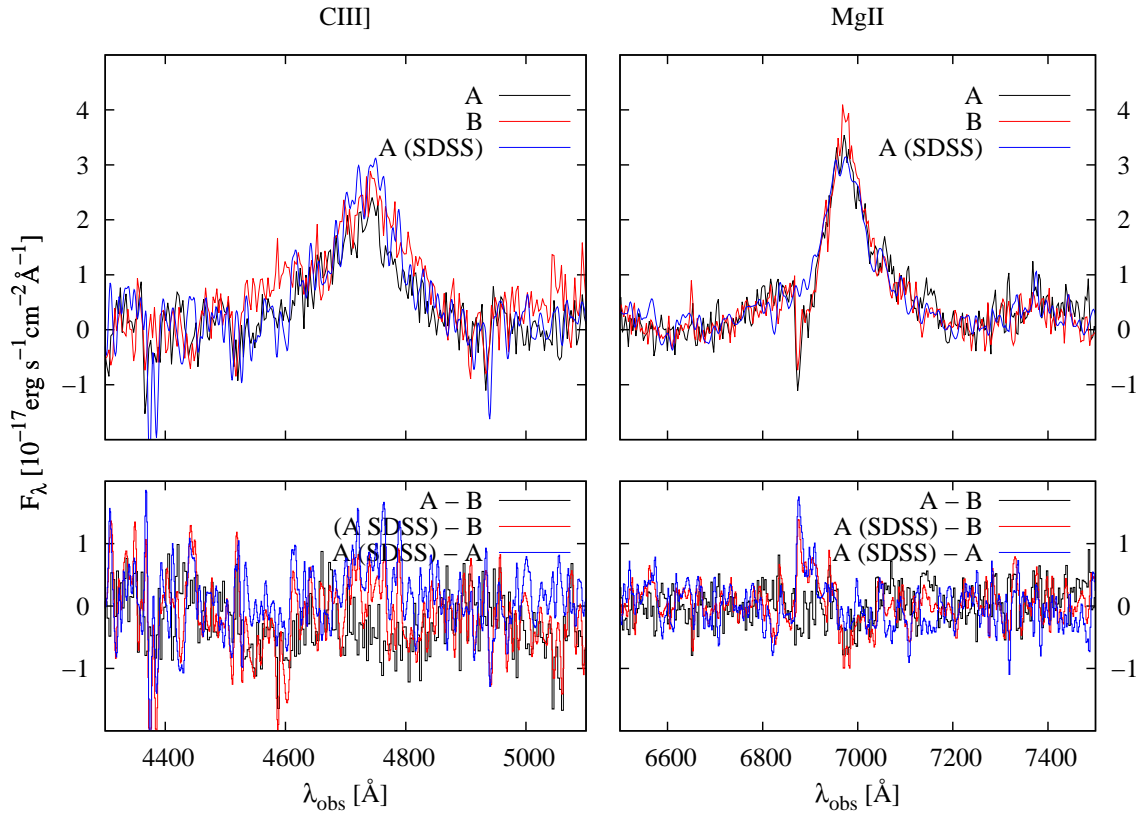


Fig. 9.— The continuum-subtracted BEL profiles of the three spectra (*top*) and their relative differences (*bottom*). The continuum was fitted by a 5th order polynomial, avoiding the regions with emission lines. The telluric absorption line at the blue wing of Mg II has been corrected out in the SDSS spectrum.

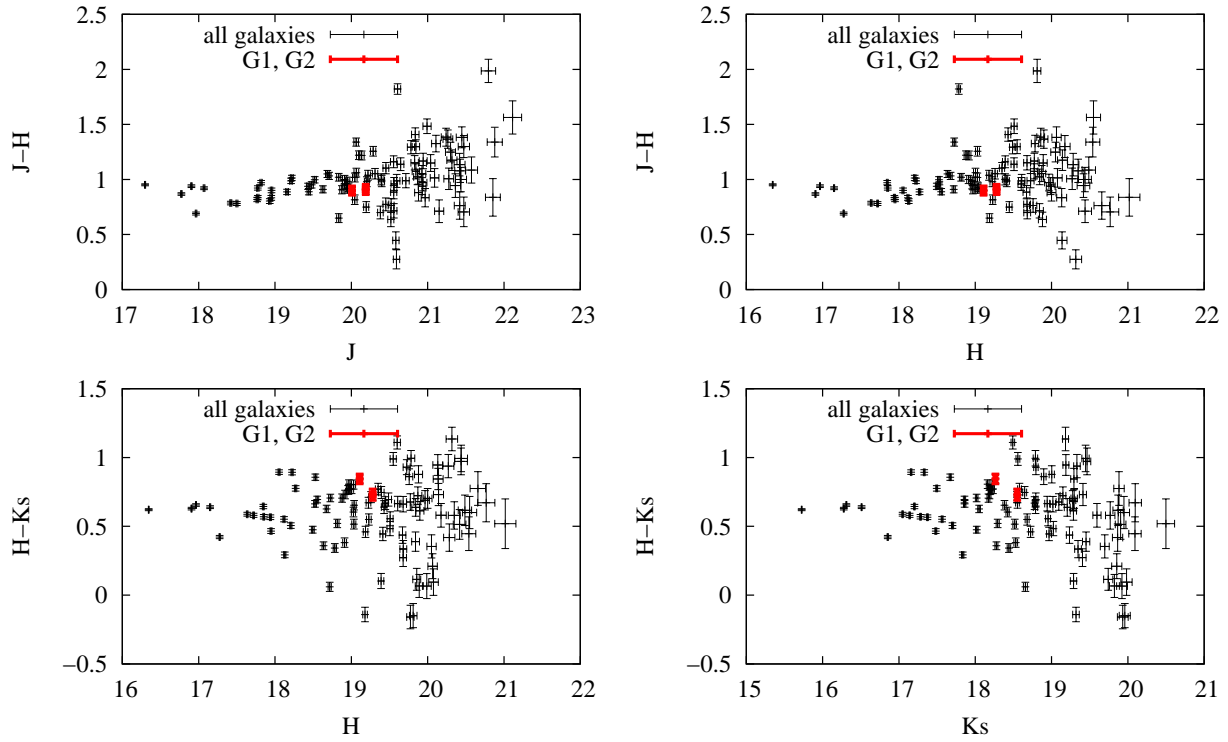


Fig. 10.— Color-magnitude diagrams for the galaxies in the complete Subaru MOIRCS field of view. We use the field of view of only one of the MOIRCS detectors, centered on the target (see the panel to the right in Figure 11). The values and error bars are aperture magnitudes (MAG_APERT) and their associated statistical uncertainties, determined with SExtractor.

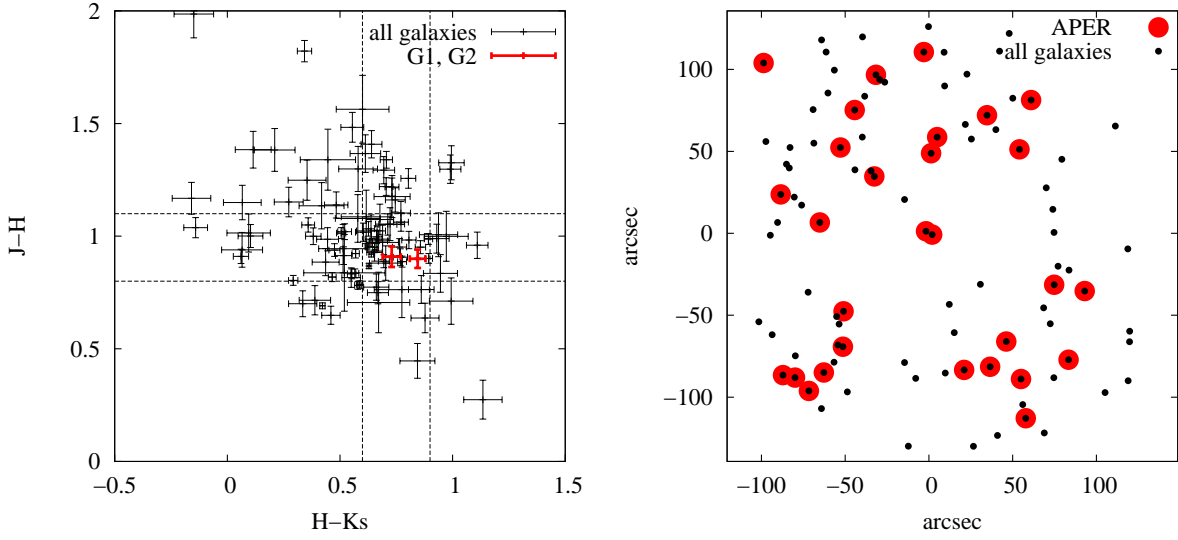


Fig. 11.— Color-color (*left*) and spatial distribution diagrams (*right*) of the galaxies in the Subaru MOIRCS field of view. The colors and associated error bars are based on aperture photometry (MAG_APERT) determined with SExtractor. The color-cut region used to isolate galaxies possibly associated with the candidate cluster at $z \sim 0.9$ is marked with dashed lines. The spatial distribution diagram identifies the galaxies whose colors match the color-cut region. We use the field of view of only one of the MOIRCS detectors, centered on the target. North is up and East is to the left. 100 arcsec at $z = 0.9$ corresponds to a proper scale of $790 h_{70}^{-1}$ kpc.

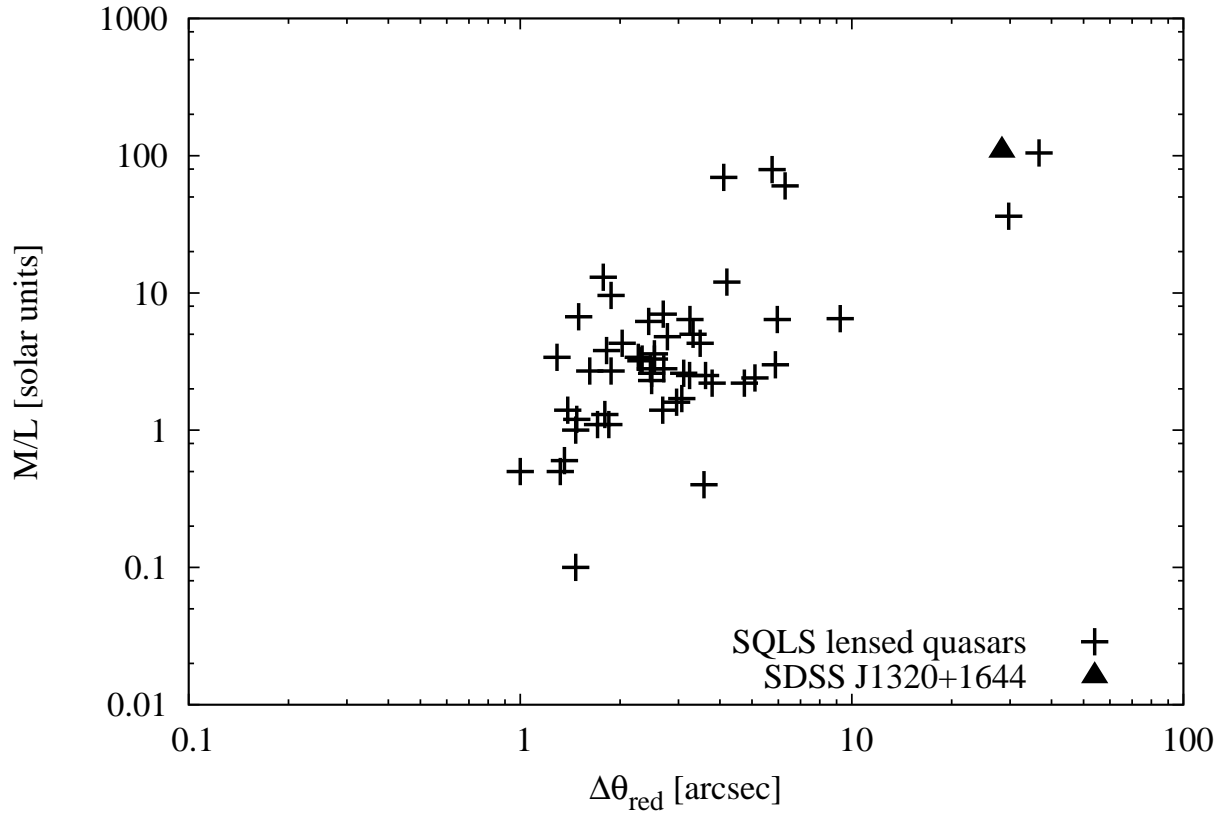


Fig. 12.— Mass-to-light ratios in the rest frame R band for 52 SQLS gravitationally lensed quasars, as well as for SDSS J1320+1644 (assuming it is also a lensed quasar). Here $\Delta\theta_{red}$ is the reduced image separation (see §7.2).